



# Numerical investigations of water-hammer with column-separation induced by vaporous cavitation using a one-dimensional Finite-Volume approach

F. Daude <sup>a,b,\*</sup>, A.S. Tijsseling <sup>c</sup>, P. Galon <sup>a,d</sup>

<sup>a</sup> IMSIA, UMR EDF-CNRS-CEA-ENSTA 9219, Université Paris-Saclay, F-91762 Palaiseau, France

<sup>b</sup> EDF R&D, ERMES, F-91120 Palaiseau, France

<sup>c</sup> Eindhoven University of Technology, Department of Mathematics and Computer Science, 5600 MB Eindhoven, The Netherlands

<sup>d</sup> CEA Saclay, DEN-SEMT, Université Paris-Saclay, F-91191, Gif-sur-Yvette, France



## ARTICLE INFO

### Article history:

Received 20 February 2018

Received in revised form 16 July 2018

Accepted 24 August 2018

### Keywords:

Water-hammer

Column-separation

Cavitation/condensation

HEM

Finite-volume method

## ABSTRACT

Water-hammer with column-separation induced by cavitation is investigated numerically. The vapor–water flow is modeled using the Homogeneous Equilibrium Model in conjunction with the 1984 NBS/NRC Steam Tables. The discretization is done with the quasi 1-D Finite-Volume approach recently developed by the authors for compressible flows in pipelines. The ability of the present approach to tackle cavitating flows is first assessed. Then, comparisons with experimental results of water-hammer with column-separation demonstrate consistency with the present computations. Based on the obtained numerical results, focus is given to the dynamics of the liquid column-separation and to the associated physics such as cavitation, vapor growth and collapse, generation of the secondary water-hammer peak and the interaction of the primary and secondary pressure waves. The influence of the initial flow velocity before valve closure on the duration and size of the cavity and on the magnitude of the secondary water-hammer is examined.

© 2018 Elsevier Ltd. All rights reserved.

## 1. Introduction

Water-hammer (WH) may occur in piping systems used in aerospace industry, hydro-power installations and nuclear reactor cooling systems. The WH phenomenon is well-studied due to its importance in designing pipe flow systems for over a century since the pioneering works of Joukowski (1900) and Allievi (1913). Extensive reviews on WH can be found in the Refs. Wylie et al. (1993), Chaudhry (2014), Ghidaoui et al. (2005) and Bergant et al. (2006). WH is the result of a sudden change of the liquid's flow velocity due to valve/pump operations or other reasons. The induced pressure variations propagate along the pipe and can damage pipes or supports disturbing the operation of the flow system. As the motion or deformation of the pipes forced by the fluid transient may strongly influence the flow in the pipe, the dynamic fluid–structure interaction should be taken into account in critical cases. In addition, the cavitation phenomenon may take place during the fast transient event when the pressure falls to the saturation value of vapor. As a consequence, the liquid starts to evaporate and column-separation may occur. Bergant et al. (2006) present a comprehensive review on the WH phenomenon with liquid column-separation. As the authors explained in this review, the collapse of vapor may induce large and steep pressure rises. In certain situations, this leads to a pressure amplitude which can be higher than the one obtained in the single liquid-phase situation given by the classical Joukowski formula. The cause of this phenomenon is the superposition of the

\* Corresponding author at: EDF R&D, ERMES, F-91120 Palaiseau, France.  
E-mail address: [frederic.daude@edf.fr](mailto:frederic.daude@edf.fr) (F. Daude).

first and the secondary pressure waves (Bergant et al., 2006). The cavitation/condensation phenomena and the interaction of several pressure waves clearly increase the complexity and severity of the fluid transient. According to Bergant and Simpson (1999), this kind of transient cavitating flow is classified as active column-separation. As reported in Bergant et al. (2006), column-separation can have a destructive effect as in the burst pipe accident at Oigawa hydropower station in 1950 in Japan (Bonin, 1960). Both experimental and numerical studies have investigated the column-separation phenomenon (Bergant et al., 2006). The existing methods for the simulation of WH with liquid column-separation are almost all 1-D and based on the Discrete Vapor Cavity Model (DVCM) using the method of characteristics as originally proposed by Wylie et al. (1993). Strong assumptions are made in the derivation of the DVCM. In particular, the vapor generated when the pressure falls to the saturation value is concentrated at the grid points and between the grid points pure liquid is assumed. As a consequence, the precise position of cavities along the pipe cannot be estimated. Another limitation lies in the inability of the cavity to move with the flow. In addition, spurious pressure spikes can be obtained using the DVCM when the mesh is sufficiently fine (Bergant et al., 2006). To alleviate this difficulty, a small amount of non-condensable gas is introduced which provides damping. This approach is referred as the Discrete Gas Cavity Model (DGCM) presented by Wylie (1984). However, the calculations are known to be sensitive to the initial assumed amount of gas. Zhou et al. (2017, 2018) recently proposed a second-order Finite-Volume approach for the water-hammer equations in which cavitation is modeled using either DVCM (Zhou et al., 2017) or DGCM (Zhou et al., 2018). This avoids the unrealistic artificial spikiness appearing on finer meshes, noting that unfiltered measurements show “spikiness” too. The first applications of Finite-Volume methods for water-hammer equations are described in Guinot (2000), Hwang and Chung (2002) and Zhao and Ghidaoui (2004). Chaiko (2006) proposed a Finite-Volume approach considering the classical conservation laws of mass and momentum instead of the linear water-hammer equations to take into account the non-linear convective terms which are significant for low wave speeds due to vapor and free gas, and thus necessary for a large range of Mach numbers. In addition, the Finite-Volume formulation ensures the discrete conservation of mass and momentum as well as the correct jump relations at discontinuities (Hirsch, 1988; Toro, 2009). Moreover, only isothermal or isentropic fluids are considered in the papers mentioned above. In this paper, non-isothermal compressible flows are considered as in realistic pipe systems the fluid temperature may vary due to heat exchange with the environment.

The numerical modeling of the cavitation phenomenon has received a lot of interest in the literature. In recent years, two-phase flow models have become popular in the modeling of cavitating flows. For example, the one-fluid model based on the assumption of mechanic, kinematic and thermodynamic equilibria treats the two-phase mixture as a single-fluid, see for example Liu et al. (2004), Zheng et al. (2013), Dumbser et al. (2013) and the references therein. As a consequence, any non-equilibrium effect cannot be taken into account and cavitation is assumed to be instantaneous. In the present paper, the one-fluid approach is retained through the use of the Homogeneous Equilibrium Model (HEM) (Clerc, 2000). The next modeling issue is to provide an adequate equation of state (EOS) for the water that covers the subcooled liquid region (where, at a given pressure, the water temperature is lower than the saturation temperature), the pure steam region (where, at a given pressure, the water temperature is higher than the saturation temperature) and the (saturated) two-phase mixture. For this purpose, the Steam Tables based on the 1984 NBS/NRC (National Bureau of Standards/National Research Council of Canada) formulation for the EOS (Haar et al., 1984) are considered herein to represent steam–water flows. In addition, the simulation of fast transients in pipe systems is usually performed using a one-dimensional approach. The quasi 1-D numerical approach presented in Daude and Galon (2018) is based on a Finite-Volume method using Godunov-type solvers and it is used for the simulation of compressible flows in flexible pipelines. In particular, the influence of the pipe hoop elasticity on the effective pressure wave speed is taken into account. Several air and water shock-type problems were tackled, involving pipe junctions, sudden changes of duct cross-section and elastic/plastic deformation of pipe walls. For example, the highly nonlinear propagation of a pressure wave in a liquid-filled pipe experiencing plastic deformation was computed and compared satisfactorily with experiments (Daude and Galon, 2018). In addition, skin friction, gravity and non-instantaneous valve closure, which are known to affect two-phase water-hammer wave evolution, are also considered here. The aim is to assess this Finite-Volume methodology through the simulation of water-hammer with column-separation and the comparison with published experimental data.

The paper is organized as follows. First, the governing equations and, then the associated numerical schemes used for the discretization are presented. Afterwards, the computation of the cavitation phenomenon is considered for 1-D theoretical Riemann problems. The numerical method is then assessed via comparison with experiments involving water-hammer with column-separation. A particular focus is on the dynamics of the water-column-separation in order to better understand where the cavitation occurs along the pipeline, how the largest vapor pocket interacts with the primary pressure wave, how the vapor pocket collapses thereby leading to a secondary water-hammer, and how the primary and the secondary WH waves interact. The influence of the initial flow velocity before valve closure on the duration of the cavity and on the severity of the secondary water-hammer is examined.

## 2. Governing equations

The Homogeneous Equilibrium Model (HEM) is used to represent two-phase flows under the following assumptions. The slip between phases is neglected and instantaneous thermal, mechanical and chemical equilibria are assumed. As a consequence the two phases share the same velocity, the same pressure, the same temperature and the same Gibbs free energy. In order to improve the modeling of the physical phenomena involved in the water-hammer events, the effect of

skin (fluid-wall) friction approximated by the steady-state Darcy–Weisbach relationship, and the pipe slope are taken into account. This leads to the following 1-D conservation equations of mass, momentum and total energy for compressible flows in ducts with variable cross-section:

$$\begin{cases} \partial_t(\rho A) + \partial_x(\rho u A) & = 0 \\ \partial_t(\rho u A) + \partial_x(\rho u^2 A + pA) - p\partial_x A & = \pi d\tau_w - \rho Ag \sin\theta \\ \partial_t(\rho e A) + \partial_x(\rho e u A + puA) + p\partial_t A & = -u\rho Ag \sin\theta \end{cases} \quad (1)$$

with  $t$  the time,  $x$  the spatial coordinate corresponding to the pipe axis,  $\rho$  the density of the mixture,  $u$  the cross-sectional average of velocity in the pipe direction,  $p$  the absolute pressure and  $e$  the specific total energy. The pipe cross-section is denoted by  $A$  and  $d$  is the inner diameter of pipe, i.e.  $A = \pi d^2/4$ . The wall shear-stress  $\tau_w$  is expressed using the quasi-steady friction term:

$$\tau_w = -\frac{1}{8}\rho f_{DW}u|u|$$

where  $f_{DW}$  is the Darcy–Weisbach friction factor. The angle of the upward pipe slope with the horizontal axis is denoted by  $\theta$  and  $g = 9.81 \text{ m s}^{-2}$  is the gravitational acceleration. The specific internal energy  $\varepsilon$  is given by:

$$\varepsilon = e - \frac{1}{2}u^2$$

It is linked to the density  $\rho$  and the absolute pressure  $p$  via an additional relation named Equation Of State (EOS):

$$\varepsilon = \varepsilon^{EOS}(\rho, p)$$

In the present work, the Steam Tables based on the 1984 NBS/NRC (National Bureau of Standards/National Research Council of Canada) formulation for the EOS (Haar et al., 1984) are retained for steam–water flows. Thermodynamic values listed in the tables are calculated from an analytic polynomial equation that is an accurate approximation to the Helmholtz function (specific Helmholtz free-energy) for ordinary (not pure) water and steam. In practice, instead of the expensive direct use of this analytic equation, a tabulation is considered at the beginning of the simulation using interpolation algorithms. Then, at each time step, determining the thermodynamic properties of steam and water as a function of absolute pressure and density from such accurate tabulation requires an iterative inversion as the steam–water tables are developed in a 3-D  $p - v - T$  diagram ( $p$  absolute pressure,  $v = 1/\rho$  specific volume and  $T$  absolute temperature). This iterative process is detailed in Lepareux (1994).

Following the assumptions of the HEM, the steam–water mixture is supposed to be at its saturation point. As a consequence, the vapor fraction  $\alpha_v$  is directly given by:

$$\alpha_v = \begin{cases} 0 & \text{when } \rho_{l,\text{sat}} \leq \rho \\ \frac{\rho - \rho_{l,\text{sat}}}{\rho_{v,\text{sat}} - \rho_{l,\text{sat}}} & \text{when } \rho_{v,\text{sat}} \leq \rho \leq \rho_{l,\text{sat}} \\ 1 & \text{when } \rho \leq \rho_{v,\text{sat}} \end{cases} \quad (2)$$

where  $\rho_{l,\text{sat}}$  and  $\rho_{v,\text{sat}}$  are the liquid and vapor densities at saturation obtained from the Steam Tables, respectively:

$$\rho_{l,\text{sat}} = \rho_{l,\text{sat}}^{EOS}(T) \quad \text{and} \quad \rho_{v,\text{sat}} = \rho_{v,\text{sat}}^{EOS}(T)$$

with the absolute temperature  $T$  given by the EOS:  $T = T^{EOS}(\rho, p)$ . As a consequence, the vapor fraction  $\alpha_v$  is directly given by the mixture density  $\rho$  and the absolute pressure  $p$  as the two-phase mixture is supposed to be at saturation, i.e.  $\alpha_v = \alpha_v(\rho, p)$ .

### 3. Numerical approach

Eq. (1) is solved using a fractional-step approach. First, the convective terms, i.e. without skin friction and gravity, are discretized using the Finite-Volume method proposed and tested for several fast transients problems in Daude and Galon (2018). This approach is based on the integral form of the Homogeneous Equilibrium Model equations applied to a time-dependent conical control volume  $V_i$  leading to the following 1-D discrete equations for a pipe with non-uniform cross-section  $A$ :

$$V_i^{n+1}\tilde{\mathbf{U}}_i - V_i^n\mathbf{U}_i^n + \Delta t^n \left( \mathbf{F}_{i+1/2}A_{i+1/2}^{n+1/2} - \mathbf{F}_{i-1/2}A_{i-1/2}^{n+1/2} \right) + p_i^n \mathbf{R}_i^n = \mathbf{0} \quad (3)$$

with

$$\mathbf{U} = \begin{pmatrix} \rho \\ \rho u \\ \rho e \end{pmatrix}, \quad \mathbf{F} = \begin{pmatrix} \rho u \\ \rho u^2 + p \\ \rho e u + pu \end{pmatrix} \quad \text{and} \quad \mathbf{R}_i^n = \begin{pmatrix} 0 \\ -\Delta t^n \left( A_{i+1/2}^{n+1/2} - A_{i-1/2}^{n+1/2} \right) \\ V_i^{n+1} - V_i^n \end{pmatrix}$$

$\mathbf{U}_i$  is the cell average of the state vector  $\mathbf{U}$ . The numerical fluxes  $\mathbf{F}_{i\pm 1/2}$  are obtained using the HLLC scheme (Toro, 2009; Toro et al., 1994). The surfaces  $A_{i\pm 1/2}^{n+1/2}$  are expressed using the inner diameters  $d$  of the pipe cell, i.e.  $A_{i\pm 1/2}^{n+1/2} = \pi \left( d_{i\pm 1/2}^{n+1/2} \right)^2 / 4$ . The conical volume  $V_i^n$  is computed by:

$$V_i^n = \frac{\pi h_i}{12} \left[ \left( d_{i+1/2}^{n-1/2} \right)^2 + d_{i+1/2}^{n-1/2} d_{i-1/2}^{n-1/2} + \left( d_{i-1/2}^{n-1/2} \right)^2 \right] \quad (4)$$

with  $h_i$  the length of the control volume  $V_i$ . The inner diameter  $d$  can be seen as an additional variable in the present fluid mechanics problem. Its FSI dynamics is detailed in the following.

The pipe wall elasticity is known to strongly affect the speed of pressure waves (Wylie et al., 1993; Chaudhry, 2014; Ghidaoui et al., 2005; Bergant et al., 2006). This is known as the Korteweg (1878) or Allievi (1913) effect. In the present work, Hooke's law describes the pipe wall hoop elasticity. Thus, the variation of the circular cross-section as a function of the change of pressure is given by the following linear relation (Tijsseling, 2007):

$$\frac{dA}{A} = \beta \frac{dp}{E} \quad \text{with} \quad \beta = \frac{2}{[(d + 2\delta)^2 - d^2]} \left[ (1 - \nu_p) d^2 + (1 + \nu_p) (d + 2\delta)^2 \right] \quad (5)$$

where  $\delta$  is the wall thickness which is assumed to be constant,  $E$  is the Young's modulus of elasticity and  $\nu_p$  is the Poisson's ratio of the pipe material. Notice that for thin-walled pipes, i.e.  $\delta \ll d$  (leading to  $\beta \approx d/\delta$ ), this relation simplifies to the following formula largely encountered in the literature (Wylie et al., 1993):

$$\frac{dA}{A} = \frac{d}{\delta} \frac{dp}{E} \quad (6)$$

Eq. (5) can be expressed in terms of the inner diameter as:

$$\frac{dd}{d} = \frac{\beta}{2} \frac{dp}{E} \quad (7)$$

or in discrete form:

$$d_{i+1/2}^{n+1/2} - d_{i+1/2}^{n-1/2} = \frac{1}{2} \beta_{i+1/2}^{n-1/2} d_{i+1/2}^{n-1/2} \frac{(p_{i+1/2}^n - p_{i+1/2}^{n-1})}{E} \quad \text{with} \quad p_{i+1/2} = \frac{V_i p_i + V_{i+1} p_{i+1}}{V_i + V_{i+1}} \quad (8)$$

Once the inner diameter is updated in accordance with the variation of pressure, both cross-sectional area  $A_{i\pm 1/2}^{n+1/2}$  and conical volume  $V_i^{n+1}$  are modified (see Eq. (4)) and used in Eq. (3) for upgrading the flow variables. In the present work, pipe stresses are assumed not to exceed the yield point. The numerical treatment of plasticity is detailed in Daude and Galon (2018).

In a second step, once the fluid variables are updated considering only the convective terms (see Eq. (3)), the skin friction is added to the momentum equation as follows:

$$\begin{cases} \widehat{\rho}_i &= \widetilde{\rho}_i \\ (\widehat{\rho u})_i &= (\widetilde{\rho u})_i + \Delta t^n \tau_w A_w / V_i^{n+1} \\ (\widehat{\rho e})_i &= (\widetilde{\rho e})_i \end{cases} \quad (9)$$

with for a straight pipe  $A_w = \pi dh$ .

In the third and final step, the gravity term is taken into account in the momentum and energy equations as:

$$\begin{cases} \rho_i^{n+1} &= \widehat{\rho}_i \\ (\rho u)_i^{n+1} &= (\widehat{\rho u})_i - \Delta t^n \widehat{\rho}_i g \sin \theta \\ (\rho e)_i^{n+1} &= (\widehat{\rho e})_i - \Delta t^n (\widehat{\rho u})_i g \sin \theta \end{cases} \quad (10)$$

The time step  $\Delta t^n$  used in Eqs. (3), (9) and (10) is given by the Courant number  $C$  defined as:

$$C = \Delta t^n \max_i \left( \frac{|u_i^n| + c_i^n}{h_i} \right) \quad (11)$$

with  $c$  the speed of sound in an unconfined fluid given by the EOS:  $c = c^{\text{EOS}}(\rho, p)$ .

As detailed in Daude and Galon (2018), the modeling of boundary conditions is based on the use of a ghost cell virtually created outside the computational domain. The fictitious state denoted here  $\bar{\mathbf{U}}$  associated with this ghost cell is then expressed using the state denoted  $\mathbf{U}_L$  of the (real) adjacent cell of the interface. Afterwards, the corresponding numerical flux is expressed using both  $\mathbf{U}_L$  and  $\bar{\mathbf{U}}$ . In real experimental setups, the valve closure cannot be considered as instantaneous. For modeling such closure, a mirror-type state is used for the corresponding boundary condition. For this purpose, the fictitious state  $\bar{\mathbf{U}}$  using for the computation of the numerical flux is expressed as:

$$\bar{\rho} = \rho_L, \quad \bar{u} = 2v(t) - u_L \quad \text{and} \quad \bar{p} = p_L \quad (12)$$

with  $v(t)$  the imposed fluid velocity at the boundary. On the one hand, the experimental measurements can be directly used for the fluid velocity history imposed via  $v(t)$  in Eq. (12). On the other hand, in the case where the experimental

measurements are not available, an analytical relation for non-instantaneous ball valve closing is considered to represent the increasing flow resistance generated during the valve closure (Tijsseling, 2003). Based on the pressure loss in steady turbulent pipe flow across a fully open valve, i.e.  $\Delta p_0 = \xi_0 \frac{1}{2} \rho u_0^2$  with  $\xi_0 = 0.2$ , and the assumed similar relation across a closing valve, i.e.  $\Delta p = \xi \frac{1}{2} \rho v^2$ , the following boundary condition is obtained (Tijsseling, 2003):

$$v(t) = \tau(t)u_0\sqrt{\frac{p}{p_0}} \quad \text{with} \quad \tau(t) = \sqrt{\frac{\xi_0}{\xi}}$$

in which the pressure downstream of the valve has been taken zero and with  $u_0$  the initial fluid velocity. Based on experimental measurements, the specific function  $\tau(t)$  used here is (Tijsseling, 2003):

$$\tau(t) = \begin{cases} \left(1 - \frac{t}{t_c}\right)^{3.53} & \text{for } 0 \leq t < 0.4t_c \\ 0.394\left(1 - \frac{t}{t_c}\right)^{1.70} & \text{for } 0.4t_c \leq t < t_c \\ 0 & \text{for } t_c \leq t \end{cases} \quad (13)$$

with  $t_c$  the valve closing time. Obviously, instantaneous valve closure is obtained with  $t_c = 0$  in Eq. (13) leading to  $v(t) = 0$  in Eq. (12) which corresponds to the classical mirror state used for rigid walls.

The other boundary condition used in the present manuscript is the tank condition detailed in Daude and Galon (2018).

All of the computations presented in the following have been performed with the fast transient dynamics software for fluids and structures Europlexus (Joint Research Centre, 2018). Europlexus is co-owned by the French Commissariat à l'énergie atomique et aux énergies alternatives (CEA) and by the European Commission. Électricité de France (EDF) is involved as a major partner of the consortium established for Europlexus software development (<http://www-epx.cea.fr>).

#### 4. Numerical tests

A selection of numerical test-cases is considered in this section. First, the ability of the present approach to compute the cavitation phenomenon is assessed with respect to 1-D Riemann problems with cavitation. Second, three different series of water-hammer experiments with column-separation are used for validation.

##### 4.1. Preliminary tests: theoretical 1-D Riemann problems with cavitation

Two 1-D cavitating Riemann problems proposed in the literature are first considered. These problems consist of two symmetric rarefaction waves. In both cases, the tube is assumed to be rigid and filled with liquid water at uniform absolute pressure  $p_0$  and uniform absolute temperature  $T_0$ . At the center of the tube, there is an initial idealized (difficult to realize in the experiments) discontinuity of velocity: two streams are moving in opposite directions with the same velocity magnitude of  $u_0$ .

##### 4.1.1. Case 1

The first case considered here is used in Dumbser et al. (2013). The tube is rigid so that its diameter  $d$  does not play a role; the initial conditions are:  $p_0 = 10^5$  Pa,  $T_0 = 298$  K and  $u_0 = 10$  m s<sup>-1</sup>. The tube is long enough (2 m herein) to avoid unwanted reflections at the boundaries of the computational domain. Transmissive (non-reflective) boundary conditions are used at the two pipe ends. The numerical solutions obtained on a very fine mesh composed of 11 000 cells and with the Courant number  $C = 0.8$  given in Eq. (11) are plotted in Fig. 1. The two rarefaction waves lead to a significant drop of the pressure so that the saturation value is reached and hence cavitation occurs in the form of a very small vapor pocket at the midpoint of the pipe. The fluctuation of temperature is negligible showing a quasi-isothermal behavior. The present numerical results are in good agreement with those obtained in Dumbser et al. (2013) on a slightly coarser grid with 10 000 cells with a third-order numerical approach (see Fig. (18) in Dumbser et al., 2013). This is observed in Fig. 1(a) and (b) where, as expected, the wave fronts obtained with the third-order numerical approach used in Dumbser et al. (2013) are sharper. Dumbser et al. used the EOS based on the IAPWS-IF97 in Dumbser et al. (2013), which is different from the one retained here based on the 1984 NBS/NRC Steam Tables. A zoom of the density and velocity profiles is provided in Fig. 2. The variation of density and velocity across the rarefaction waves located at  $x \approx 1.75$  m (and at  $x \approx 0.25$  m by symmetry) is clearly visible, whereas the void fraction is constant and equal to zero (see Fig. 1(f)) as the density remains higher than the liquid density at saturation (see Eq. (2)). The velocity jump can be estimated as follows. Based on the initial conditions, the values of density, speed of sound and saturation pressure given by the Steam Tables are:  $\rho_0 = 997.15$  kg m<sup>-3</sup>,  $c_0 = 1500.87$  m s<sup>-1</sup> and  $p_{\text{sat}} = 3170$  Pa. In the same manner, the liquid and vapor densities at saturation are also given by the Steam Tables:  $(\rho_{l,\text{sat}})_0 = 997.04$  kg m<sup>-3</sup> and  $(\rho_{v,\text{sat}})_0 = 0.023$  kg m<sup>-3</sup>, leading to the initial void fraction  $(\alpha_v)_0 = 0$  as  $\rho_0 > (\rho_{l,\text{sat}})_0$ . Then, assuming that the density and the speed of sound are constant across the pure liquid rarefaction waves, the Joukowsky relation (Joukowsky, 1900) can be used. This leads to the following estimation of the velocity jump across the rarefaction waves:  $\Delta u = (p_0 - p_{\text{sat}})/(\rho_0 c_0) \approx 0.065$  m s<sup>-1</sup> which is exactly the value observed in Fig. 2(b). In addition, the wave fronts propagating at the constant speed  $u_0 + c_0$  traveled a distance of 0.75 m at  $t = 0.5$  ms.

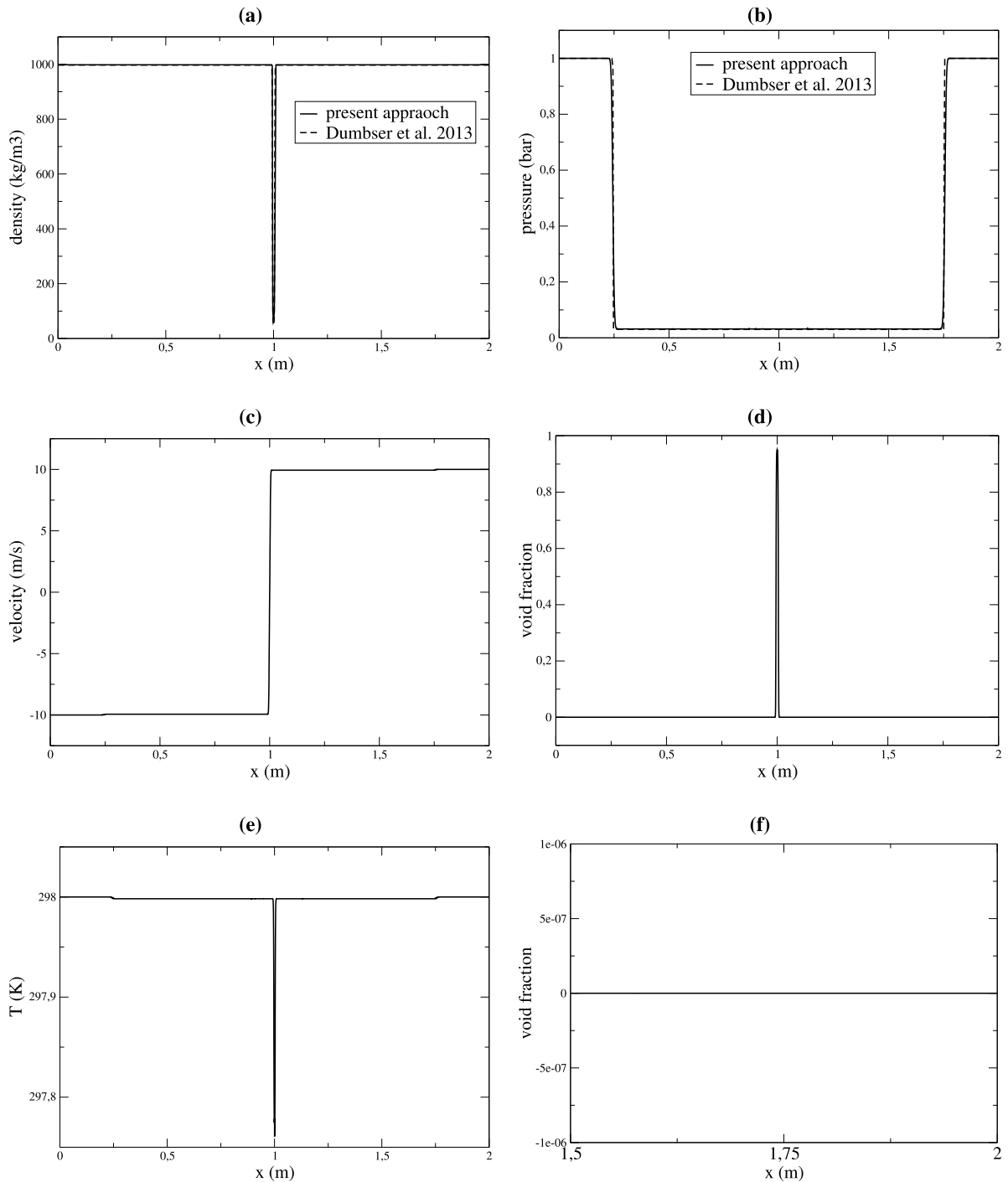


**Fig. 1.** Numerical solutions obtained with 11 000 cells and  $c = 0.8$  for the first cavitating Riemann problem: density (a); pressure (b); velocity (c); void fraction; (d) temperature (e) profiles and zoom of the void fraction profile (f) at  $t = 0.5$  ms.

#### 4.1.2. Case 2

The second case considered here and used in Liu et al. (2004) and Zheng et al. (2013) is similar to the previous case. The tube is rigid and the (explosive type) initial conditions are:  $p_0 = 10^8$  Pa,  $T_0 = 293.15$  K and  $u_0 = 100$  m s<sup>-1</sup>. The length of the tube is set to be 1 m. Once again, transmissive boundary conditions are used at the terminals of the tube. The numerical solutions obtained with 5000 cells and the Courant number  $C = 0.8$  in Eq. (11) are plotted in Fig. 3. As in Case 1, the

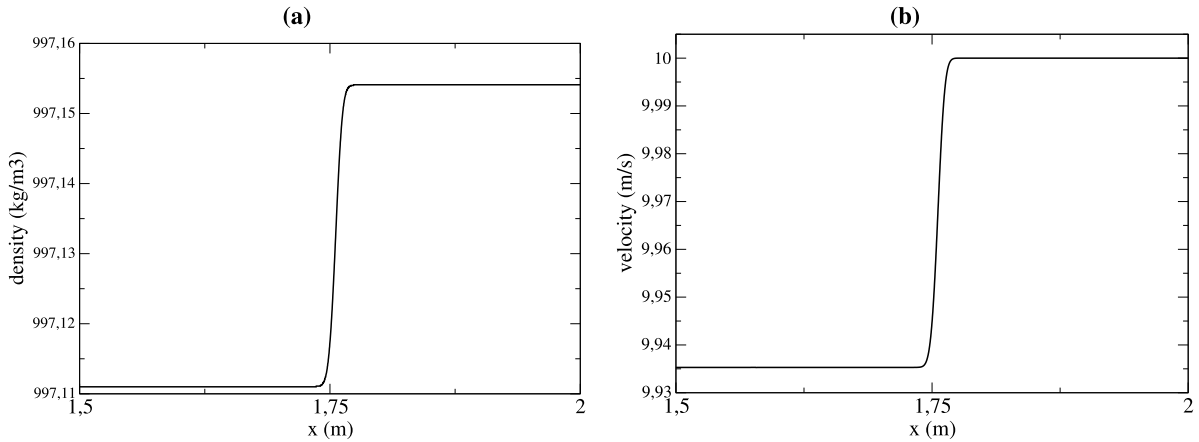


**Fig. 2.** Numerical solutions obtained with 11 000 cells and  $c = 0.8$  for the first cavitating Riemann problem: zoom of the density (a) and velocity (b) profiles at  $t = 0.5$  ms.

pressure decreases due to the two rarefaction waves and reaches the saturation value. The water at the midpoint of the tube evaporates and forms a large vapor pocket. A cavitating region ( $0.49 \text{ m} < x < 0.51 \text{ m}$ ) is needed to accommodate the void generated. The density in this region drops drastically and the void fraction increases strongly. This cavitating region is small in comparison to the size of the zone where the pressure reaches the saturation value ( $0.2 \text{ m} < x < 0.8 \text{ m}$  at  $t = 0.2 \text{ ms}$ ) showing that having the pressure dropped to vapor pressure is not a sufficient condition for the inception of cavitation. The variation of the density and velocity across the two symmetric rarefaction waves (located at  $x \approx 0.2 \text{ m}$  and at  $x \approx 0.8 \text{ m}$  at  $t = 0.2 \text{ ms}$ ) are clearly visible in contrast to the previous case where they were only visible in the zoom-in displayed in Fig. 2(a) and (b). This difference is due to the much larger initial velocity which strongly increases the strength of the rarefaction waves in the present case. This leads to a larger vapor pocket generated at the midpoint of the tube in comparison with the previous case (see Figs. 1(d) and 3(d)). Contrary to Case 1, the velocity jump cannot be estimated with the Joukowski relation. The initial values of density, speed of sound and saturation pressure given by the Steam Tables using the initial conditions are:  $\rho_0 = 1039.88 \text{ kg m}^{-3}$ ,  $c_0 = 1629.74 \text{ m s}^{-1}$  and  $p_{\text{sat}} = 2340 \text{ Pa}$ . In the same manner, the liquid and vapor densities at saturation are also given by the Steam Tables:  $(\rho_{l,\text{sat}})_0 = 998.16 \text{ kg m}^{-3}$  and  $(\rho_{v,\text{sat}})_0 = 0.017 \text{ kg m}^{-3}$ , leading to the initial void fraction  $(\alpha_v)_0 = 0$ . The Joukowski formula leads to the following estimation:  $\Delta u = (p_0 - p_{\text{sat}})/(\rho_0 c_0) \approx 59 \text{ m s}^{-1}$ . This is slightly different from the numerical results. Due to the strong density variation across the rarefaction waves, the Joukowski relation is still not valid; this explains the observed discrepancies. Finally, the head of each two rarefaction waves propagating at the speed  $u_0 + c_0$  traveled a distance of  $0.35 \text{ m}$  at  $t = 0.2 \text{ ms}$ . The numerical results obtained here are in agreement with those of Zheng et al. (2013) (see Fig. (6) in Zheng et al., 2013) as seen in Fig. 3(a) and (b) showing the ability of the present approach to simulate the cavitation phenomenon in a satisfactory manner even for such an extreme test-case. The pressure fronts of the two rarefaction waves are sharper in the present study due to the cell refinement: 1000 cells herein versus 400 cells in Zheng et al. (2013). In addition, the EOS are different: analytical Tait equation in Zheng et al. (2013) and Steam Tables based on the 1984 NBS/NRC formulation herein. Therefore the intermediate states are not exactly the same in the two computations and this is slightly visible in the density profile.

The present mathematical model and numerical method are now assessed on experimental cases involving cavitation. For this purpose, three well-documented experimental set-ups used to study liquid column-separation are considered.

#### 4.2. Simpson's column-separation water-hammer experiments

Simpson (1986) and Simpson and Wylie (1991) has conducted a range of experiments to study the generation of cavitation during a water-hammer event. The water-hammer phenomenon is initiated by the sudden closure of a valve located at the end of a pipe carrying a steady flow of water. By varying the initial flow velocity, the generation of cavitation and the strength of the water-hammer are strongly modified. Three cases are investigated in the present work. Because of the presence of fixed supports that are located at several points of the experimental apparatus, the FSI junction coupling mechanism is expected to be negligible. That is why the experimental set-up is here modeled using an ideal tank-pipe-valve system. The copper pipe is  $36 \text{ m}$  long, with an inner diameter of  $d = 19 \text{ mm}$  and a wall thickness of  $\delta = 1.6 \text{ mm}$ , and rises  $1 \text{ m}$  over the total length of  $36 \text{ m}$  which corresponds to a pipe inclination angle of  $\theta = 1.59^\circ$  as sketched in Fig. 4. The fluid pressure is measured at three positions along the pipe. The inlet boundary condition represents the tank imposing its own constant pressure  $p_{\text{tank}}$  (setting to be equal to the initial pressure  $p_0$  at position  $x = 0 \text{ m}$ ) during the transient, whereas the outlet boundary condition represents the non-instantaneous closure of the ball valve. The initial conditions for the fluid and the material properties for the pipe wall used in the computations of the three experiments are given in Table 1.  $f_{\text{DW}}$  is the

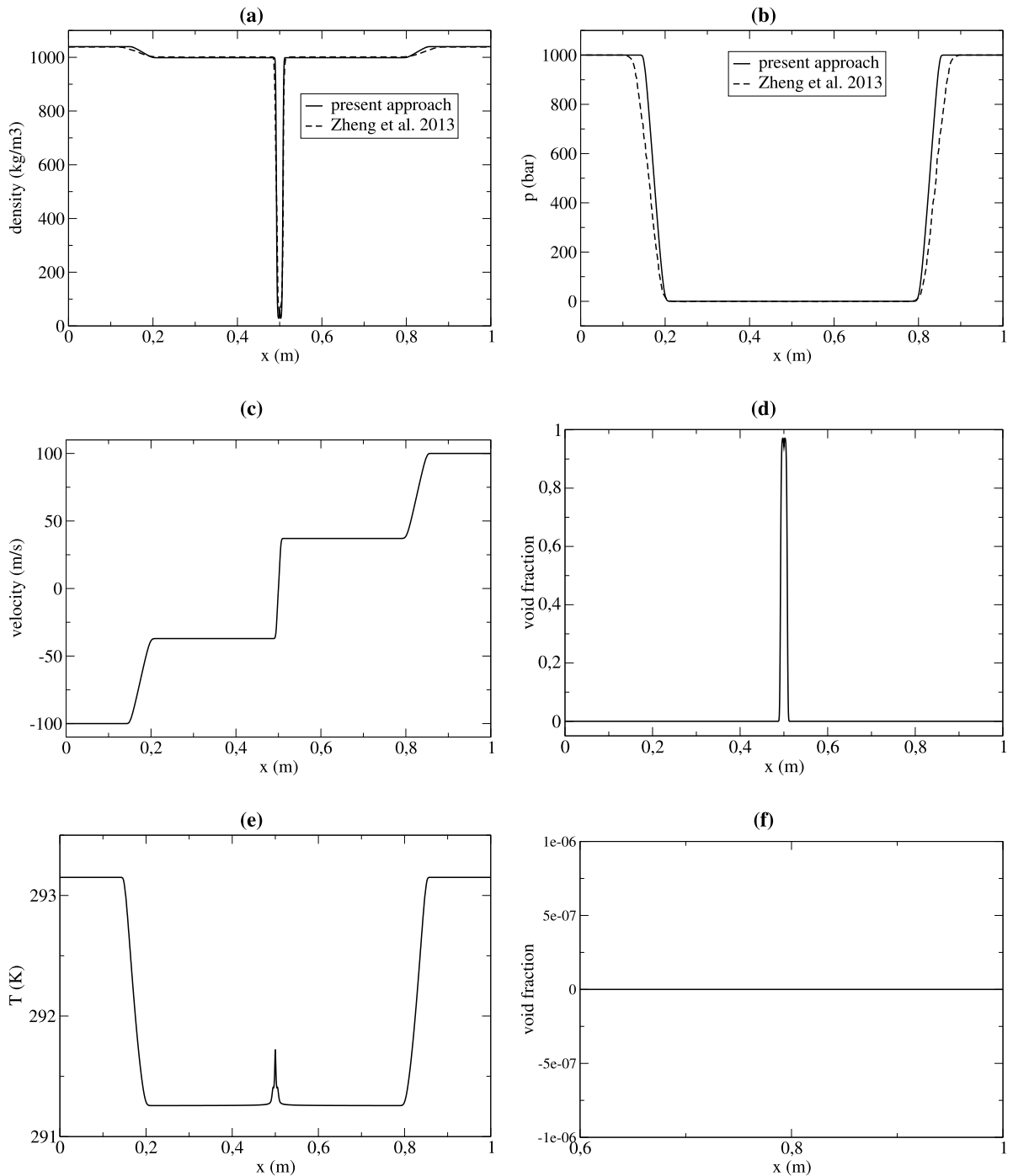


**Fig. 3.** Numerical solutions obtained with 5000 cells and  $c = 0.8$  for the second cavitating Riemann problem: density (a); pressure (b); velocity (c); void fraction (d); temperature (e) and zoom of the void fraction (f) profiles at  $t = 0.2$  ms.

measured Darcy–Weisbach friction factor used in Eq. (9). The non-instantaneous valve closure is modeled using Eq. (12) and the experimental fluid velocity history listed in Appendix A. The present computations take into account the gravity effect induced by the pipe inclination. In the three experiments performed by Simpson, the initial absolute temperature and initial absolute pressure given in Table 1 correspond to the following density, speed of sound and saturation pressure which are

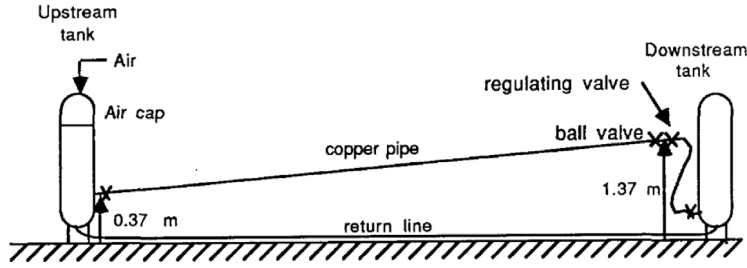


Fig. 4. Sketch of Simpson's experimental apparatus from Simpson (1986).

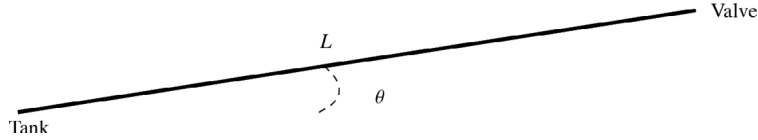


Fig. 5. One-dimensional representation of the valve closure experiment composed of a straight pipe of length  $L$  with a constant upward pipe slope of  $\theta$ , connecting a tank and a valve.

given by the Steam Tables:

$$\rho_0 = \rho^{\text{EOS}}(p_0, T_0) = 997.38 \text{ kg m}^3, \quad c_0 = c^{\text{EOS}}(p_0, T_0) = 1496.9 \text{ m s}^{-1} \quad \text{and} \quad p_{\text{sat}}^{\text{EOS}}(T_0) = 0.03 \text{ bar}$$

In the same manner, the liquid and vapor densities at saturation are also given by the Steam Tables:

$$\rho_{l,\text{sat}}^{\text{EOS}}(T_0) = 997.26 \text{ kg m}^3 \quad \text{and} \quad \rho_{v,\text{sat}}^{\text{EOS}}(T_0) = 0.022 \text{ kg m}^3$$

According to Eq. (2), as  $\rho_0 > \rho_{l,\text{sat}}^{\text{EOS}}(T_0)$ , the initial conditions are in pure liquid-phase, i.e.  $(\alpha_v)_0 = 0$  as reported in Table 1. The Young's modulus of elasticity used in the present computations is the same as the one used in the computations performed by Gale and Tiselj (2002) in order to retrieve the measured speed of the pressure waves. This leads to the value  $E = 75 \times 10^3 \text{ MPa}$  reported in Table 1 instead of the value  $E = 119 \times 10^3 \text{ MPa}$  given by the copper material properties. Indeed, using the Korteweg formula (Korteweg, 1878) for the effective speed of sound:

$$\tilde{c}_0^2 = \frac{c_0^2}{1 + \frac{\rho_0 \beta c_0^2}{E}} \quad \text{where} \quad \beta = \frac{2}{[(d + 2\delta)^2 - d^2]} [(1 - \nu_p) d^2 + (1 + \nu_p) (d + 2\delta)^2] \quad (14)$$

leads to the following value:  $\tilde{c}_0 = 1263 \text{ m s}^{-1}$  which corresponds with an error of 1.3% to the measurement of Simpson:  $\tilde{c}_{\text{exp}} = 1280 \text{ m s}^{-1}$ . This speed of sound is then used in the Joukowsky relation (Joukowsky, 1900):

$$\Delta p = \pm \rho_0 \tilde{c}_0 \Delta u \quad (15)$$

which gives the magnitude of the pressure jump due to the water-hammer. The wave reflection time is given by:

$$\mathcal{T} = \frac{2L}{\tilde{c}_0} \quad (16)$$

which corresponds here to  $\mathcal{T} \approx 57 \text{ ms}$ . The initial pressure gradient in the pipe due to skin friction and gravity is taken into account in the following initial condition (neglecting the effect of the pressure gradient on the liquid density):

$$p(x, t = 0) = p_0 - \rho_0 x \left( \frac{f_{\text{DW}}}{2d} u_0 |u_0| + g \sin \theta \right) \quad \text{for } 0 \leq x \leq L \quad (17)$$

The 1-D problem considered in the following is represented in Fig. 5. All of the computations presented in the following have been performed using 1000 cells to ensure grid-converged results and the Courant number  $C = 0.8$  in Eq. (11) which corresponds to a time step of  $\Delta t = 1.92 \times 10^{-5} \text{ s}$ .

#### 4.2.1. Case 1: single phase ( $u_0 = 0.239 \text{ m s}^{-1}$ and $p_0 = 3.469 \text{ bar}$ )

In this case, the water in the entire pipe remains in pure liquid-phase during all the transient event. The numerical results are compared with the experiments in Fig. 6. Pressure histories at different locations along the pipe (near the valve at  $x = L$ , at  $x = 3L/4$  and at  $x = L/4$ ) and the void fraction history near the valve are shown here. A good agreement is obtained because the speed of pressure waves  $\tilde{c}_0$  in the computation corresponds to the measured value as the inner diameter of the pipe follows the pressure according to Eq. (8). As expected, the simulated pressure history is periodic with

**Table 1**

Flow initial conditions and wall material properties for three of Simpson's pipe column-separation water-hammer experiments.

Case	$p_0$ (Pa)	$T_0$ (K)	$(\alpha_v)_0$	$u_0$ (m s <sup>-1</sup> )	$f_{bw}$	$L$ (m)	$d$ (m)	$\delta$ (m)	$E$ (MPa)	$\nu_p$
1	$3.469 \times 10^5$	297	0	0.239	0.0325					
2	$3.281 \times 10^5$	297	0	0.401	0.0290	36.0	$19 \times 10^{-3}$	$1.6 \times 10^{-3}$	$75 \times 10^3$	0.3
3	$3.118 \times 10^5$	297	0	1.125	0.0230					

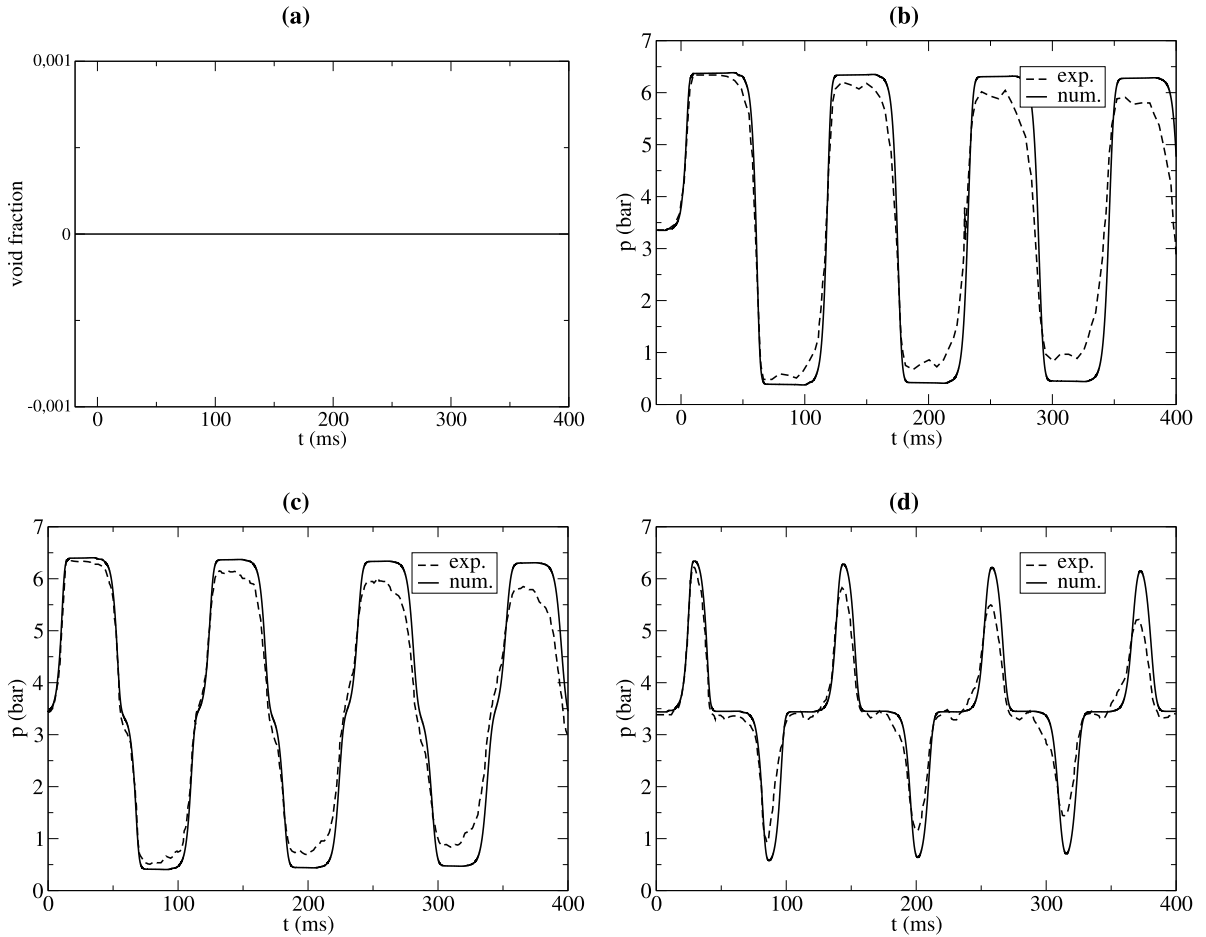


**Fig. 6.** Comparison between numerical solutions obtained with 1000 cells and  $c = 0.8$ ,  $\Delta t = 1.92 \times 10^{-5}$  s, and the data of Simpson's water-hammer experiment with  $u_0 = 0.239$  m s<sup>-1</sup>: void fraction history (a) at  $x = L$  (valve); pressure history (b) at  $x = L$  (valve); (c) at  $x = 3L/4$ ; (d) at  $x = L/4$ .

period  $\mathcal{T} = 2L/\tilde{c}_0 \approx 57$  ms. As the water remains in single-phase, a single pressure wave whose magnitude is given by the Joukowski formula (Joukowski, 1900) ( $p_{\max} = p_0 + \rho_0 \tilde{c}_0 u_0 \approx 6.48$  bar and  $p_{\min} = p_0 - \rho_0 \tilde{c}_0 u_0 \approx 0.46$  bar  $> p_{\text{sat}}$ ) propagates up and down along the pipe. The predicted pressure attenuation is found to be too low in comparison with the experiments. According to Bughazem and Anderson (2000) and Bergant et al. (2001, 2008a, b), the use of a quasi-steady friction model is not sufficient to correctly reproduce the wall friction effects in transient flows, in particular in regions of vaporous cavitation where the pressure gradient is zero. Friction losses depending on the instantaneous flow acceleration must be taken into account. It is expected that the incorporation of unsteady friction modeling can further improve the shape and timing of the pressure signal. Since turbulence is not part of the current study, the related subject of unsteady friction has been left out. Finally, the fluctuation of temperature is negligible.

#### 4.2.2. Case 2: moderate cavitation ( $u_0 = 0.401$ m s<sup>-1</sup> and $p_0 = 3.281$ bar)

In this second experiment, the initial velocity is increased in comparison with the previous case. This induces a first pressure peak which is also increased and after wave reflection it causes cavitation at the valve. The comparison between the experimental data obtained by Simpson and the present numerical results are plotted in Fig. 7. Pressure histories at different locations along the pipe and the void fraction history near the valve show again a good agreement between the numerical results and the experiments. In this case, the reflection of the rarefaction wave at the valve at  $t = \mathcal{T} = 2L/\tilde{c}_0 \approx 57$  ms

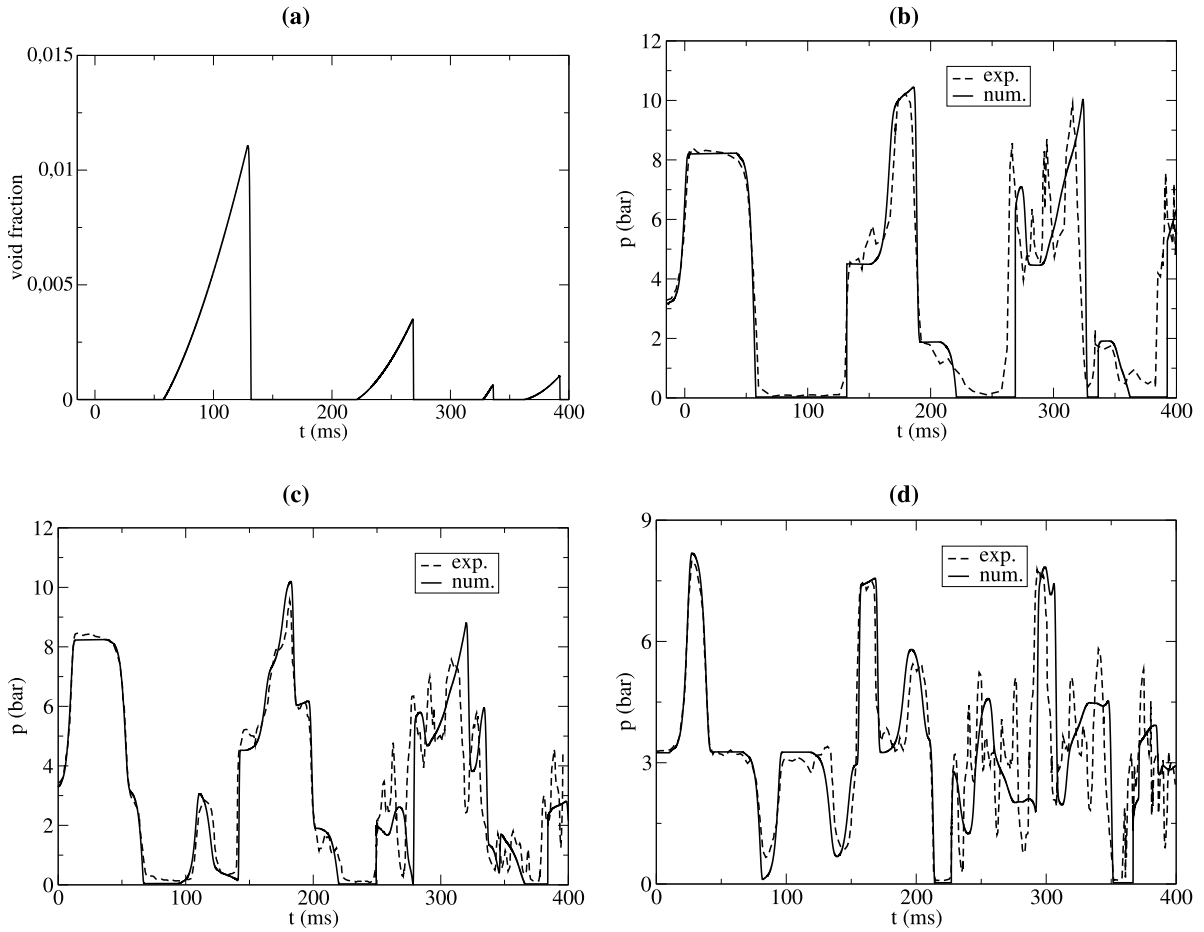


**Fig. 7.** Comparison between numerical solutions obtained with 1000 cells and  $c = 0.8$ ,  $\Delta t = 1.92 \times 10^{-5}$  s, and the data of Simpson's water-hammer experiment with  $u_0 = 0.401$  m s $^{-1}$ : void fraction history (a) at  $x = L$  (valve); pressure history (b) at  $x = L$  (valve); (c) at  $x = 3L/4$ ; (d) at  $x = L/4$ .

induces a pressure drop down to the saturation value. Thus water cavitation occurs near the valve and vapor appears. Afterwards, at  $t = \tau_0 \approx 135$  ms, this vapor void collapses at the valve thereby generating a second pressure wave which will interact with the first one. This leads to a pressure peak at the valve at  $t = 6L/\tilde{c}_0 \approx 171$  ms which is higher than the initial pressure amplitude (due to the sudden closure of the valve). In other words, in this cavitating transient event the maximum overpressure is higher than the classical Joukowski value. There is a strong correlation between pressure and void fraction near the valve. When the pressure reaches the saturation value at the valve, vapor is generated gradually (nearly linear) and when the vapor disappears nearly instantaneously (see Fig. 7(a)), this generates a new pressure wave. In order to better understand the physical phenomena occurring during column-separation, a detailed analysis is given in Appendix B based on frictionless computations. The oscillations observed in the third experimental pressure peak at the valve for  $275$  ms  $< t < 325$  ms may be linked to valve vibration and wave propagation in the downstream pipe, which is not taken into account in the present computation, and partly to the stochastic nature of cavitation. These may also explain the discrepancies observed between numerics and experiments when  $t > 200$  ms.

#### 4.2.3. Case 3: severe cavitation ( $u_0 = 1.125$ m s $^{-1}$ and $p_0 = 3.118$ bar)

The third experiment performed by Simpson and simulated here is characterized by an extensive vaporous cavitation at the valve. The numerical results are compared with the experiments in Fig. 8. A good agreement is obtained for the pressure peaks; the first one corresponds to the classical Joukowski amplitude ( $p = p_0 + \rho_0 \tilde{c}_0 u_0 \approx 17.29$  bar) and the second is due to cavity collapse. A larger size and a longer duration of cavity is obtained due to the larger initial water velocity. At  $x = L/4$  five plateaus appear where the pressure drops to a value close to the saturation value and five plateaus where it is at a value close to the tank pressure (between the two main pressure peaks). This corresponds exactly to the propagation of the primary water-hammer wave between the valve and the tank. At the two boundaries of the pipe, i.e. the valve and the tank, the pressure is imposed at the tank pressure at  $x = 0$  and at the saturation pressure at  $x = L$  due to cavitation. Once again, the vapor condensates nearly instantaneously (see Fig. 8(a)). While the primary pressure wave due to valve

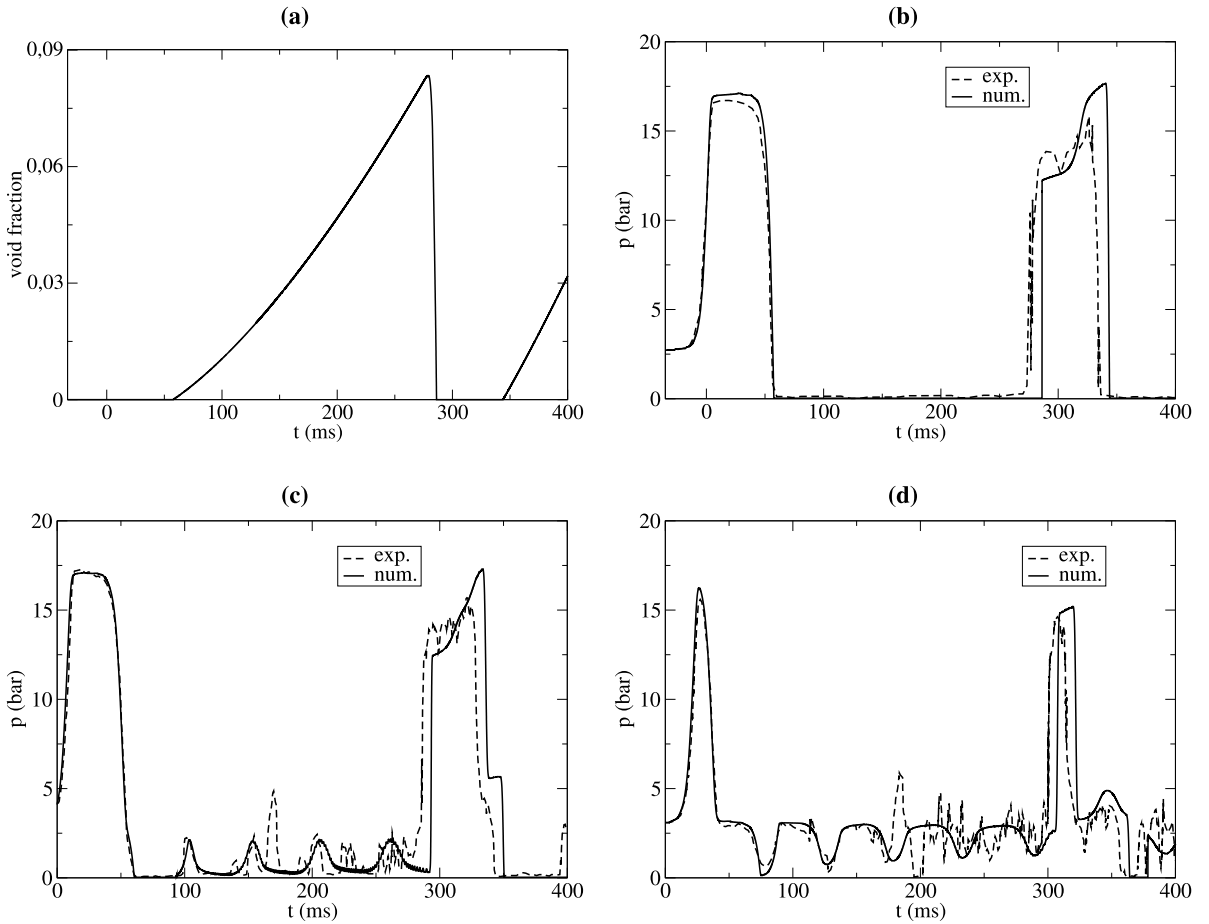


**Fig. 8.** Comparison between numerical solutions obtained with 1000 cells and  $c = 0.8$ ,  $\Delta t = 1.92 \times 10^{-5}$  s, and the data of Simpson's water-hammer experiment with  $u_0 = 1.125 \text{ m s}^{-1}$ : void fraction history (a) at  $x = L$  (valve); pressure history (b) at  $x = L$  (valve); (c) at  $x = 3L/4$ ; (d) at  $x = L/4$ .

closure is well captured, both timing and shape of the second pressure wave due to cavity collapse are quite altered. In this high-initial-velocity case, the influence of friction losses and cavitation stochastics is larger than in the two previous cases.

No spurious pressure oscillations are observed in any of the present three computations even with the use of fine meshes involving 1000 cells. The influence of the initial flow velocity on the first cavitation is studied in [Appendix C](#).

#### 4.3. Bergant and Simpson's column-separation water-hammer experiments

Another but similar set of experiments was conducted by [Bergant and Simpson \(1999\)](#). The copper pipe is 37.2 m long with an inner diameter of 22 mm, a wall thickness of  $\delta = 1.6$  mm and a constant upward pipe slope  $\theta = 3.2^\circ$ . The initial conditions of the two experiments considered herein are given in [Table 2](#). Time  $t_c$  is the valve closure time to be used in Eqs. (12) and (13). The initial absolute pressure and absolute temperature correspond to the following density, speed of sound and saturation pressure:

$$\rho_0 = \rho^{\text{EOS}}(p_0, T_0) = 999.06 \text{ kg m}^{-3}, \quad c_0 = c^{\text{EOS}}(p_0, T_0) = 1475.28 \text{ m s}^{-1} \quad \text{and} \quad p_{\text{sat}}^{\text{EOS}}(T_0) = 0.018 \text{ bar}$$

In the same manner, the liquid and vapor densities at saturation are also given by the Steam Tables:

$$\rho_{l,\text{sat}}^{\text{EOS}}(T_0) = 998.9 \text{ kg m}^{-3} \quad \text{and} \quad \rho_{v,\text{sat}}^{\text{EOS}}(T_0) = 0.014 \text{ kg m}^{-3}$$

Once again, according to Eq. (2), as  $\rho_0 > \rho_{l,\text{sat}}^{\text{EOS}}(T_0)$ , the initial conditions are in pure liquid-phase, i.e.  $(\alpha_v)_0 = 0$  as reported in [Table 2](#). Using the Korteweg formula (Eq. (14)) for the wave speed gives  $\tilde{c}_0 = 1302.36 \text{ m s}^{-1}$  which is within 1.3% of error in comparison to the measurement of Bergant & Simpson:  $\tilde{c}_{\text{exp.}} = 1319 \text{ m s}^{-1}$ .

Then, the speed of pressure waves is used in the Joukowski relation (Eq. (15) and the wave reflection time (Eq. (16)) is  $\mathcal{T} \approx 57$  ms. The initial pressure gradient due to skin friction and gravity is taken into account via Eq. (17). Once again,

**Table 2**  
Initial conditions for two of Bergant and Simpson’s pipe column-separation water-hammer experiments.

Case	$p_0$ (Pa)	$T_0$ (K)	$(\alpha_v)_0$	$u_0$ (m s <sup>-1</sup> )	$f_{DW}$	$t_c$ (ms)	$L$ (m)	$d$ (m)	$\delta$ (m)	$E$ (MPa)	$\nu_p$
1	$2.93 \times 10^5$	289.1	0	0.3	0.0258	9	37.2	$22 \times 10^{-3}$	$1.6 \times 10^{-3}$	$119 \times 10^3$	0.34
2	$2.93 \times 10^5$	289.1	0	1.4	0.0114	9					

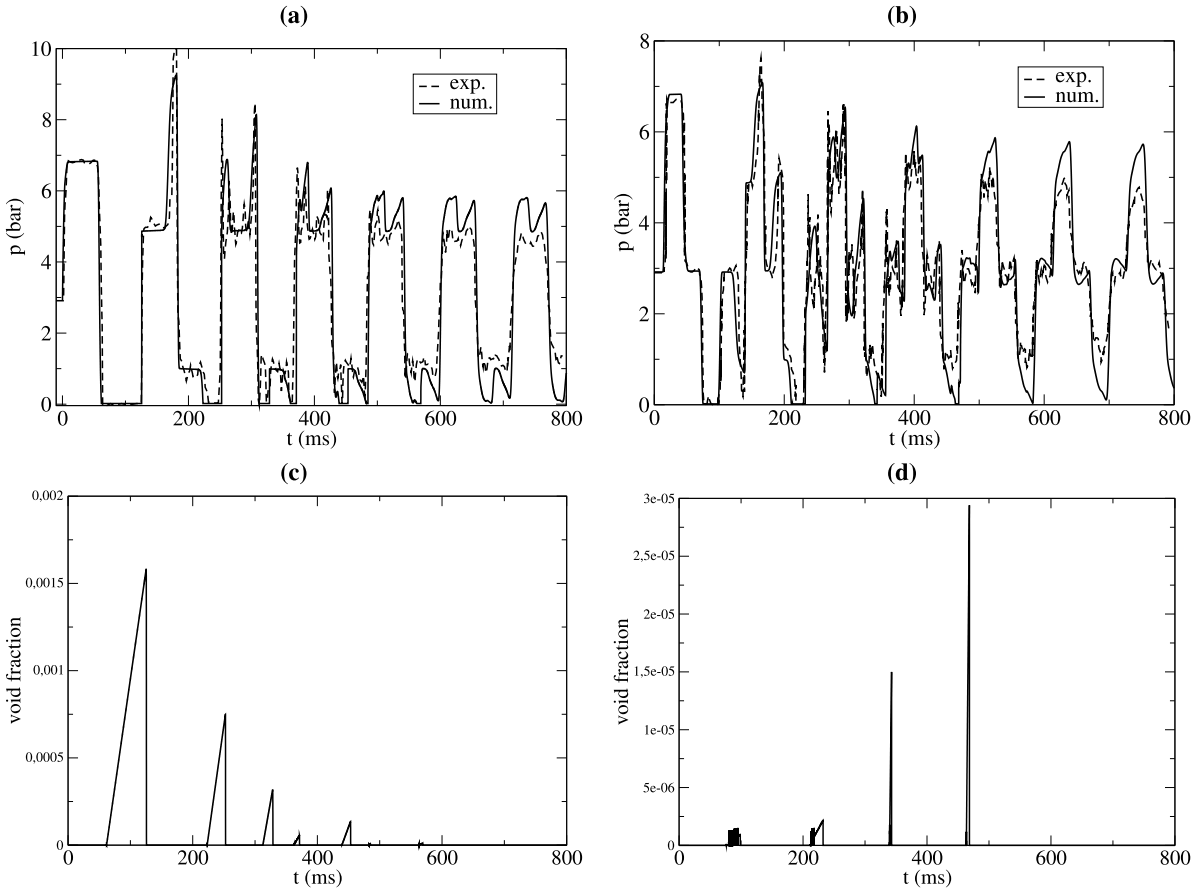


**Fig. 9.** Comparison between numerical solutions obtained with 1000 cells and  $c = 0.8$ ,  $\Delta t = 2 \times 10^{-5}$  s, and the data of Bergant & Simpson’s water-hammer experiment with  $u_0 = 0.3$  m s<sup>-1</sup>: pressure history (a) at  $x = L$  (valve) and (b) at  $x = L/2$ ; void fraction history (c) at  $x = L$  (valve) and (d) at  $x = L/2$ .

a non-instantaneous valve closure is considered. The same 1-D configuration as previously is considered in the following (see Fig. 5). All of the computations presented in the following have been performed using 1000 cells to have once again grid-converged results and a Courant number  $c = 0.8$  in Eq. (11) which corresponds to a time step of  $\Delta t = 2 \times 10^{-5}$  s.

4.3.1. Case 1: moderate cavitation ( $u_0 = 0.3$  m s<sup>-1</sup>)

This experimental case corresponds to a water-hammer with moderate cavitation. The histories of pressure and void fraction are presented in Fig. 9 at the valve and at the middle of the pipe. The numerical pressure history is compared to its experimental counterpart and shows good agreement. The first pressure peak generated by the closure of the valve corresponds to the Joukowski value:  $p = p_0 + \rho_0 \tilde{c}_0 u_0 \approx 6.83$  bar. Afterwards, cavitation occurs at the valve due to the reflection of the rarefaction wave at  $t = 2L/\tilde{c}_0 \approx 57$  ms, i.e. the pressure drops to the saturation value. The vapor zone collapses at  $t = \tau_0 \approx 120$  ms and generates the second water-hammer. Then, the combination of the first and the second water-hammer transients leads to a pressure peak at  $t = 6L/\tilde{c}_0 \approx 171$  ms at the valve which magnitude of  $p \approx 10.1$  bar is higher than the Joukowski pressure (Eq. (15)). The end of this pressure pulse corresponds to the arrival of the second water-hammer wave at the valve at  $t = \tau_0 + 2L/\tilde{c}_0 \approx 177$  ms. This very short duration of 6 ms demonstrates the accuracy of the numerical method used here. The three last pressure peaks are overestimated even with the consideration of quasi-steady wall friction. However, the timing of the pressure waves is well retrieved by the computation even for the later water-hammer events (for  $t > 700$  ms). Once again, the fluctuation of temperature is negligible.

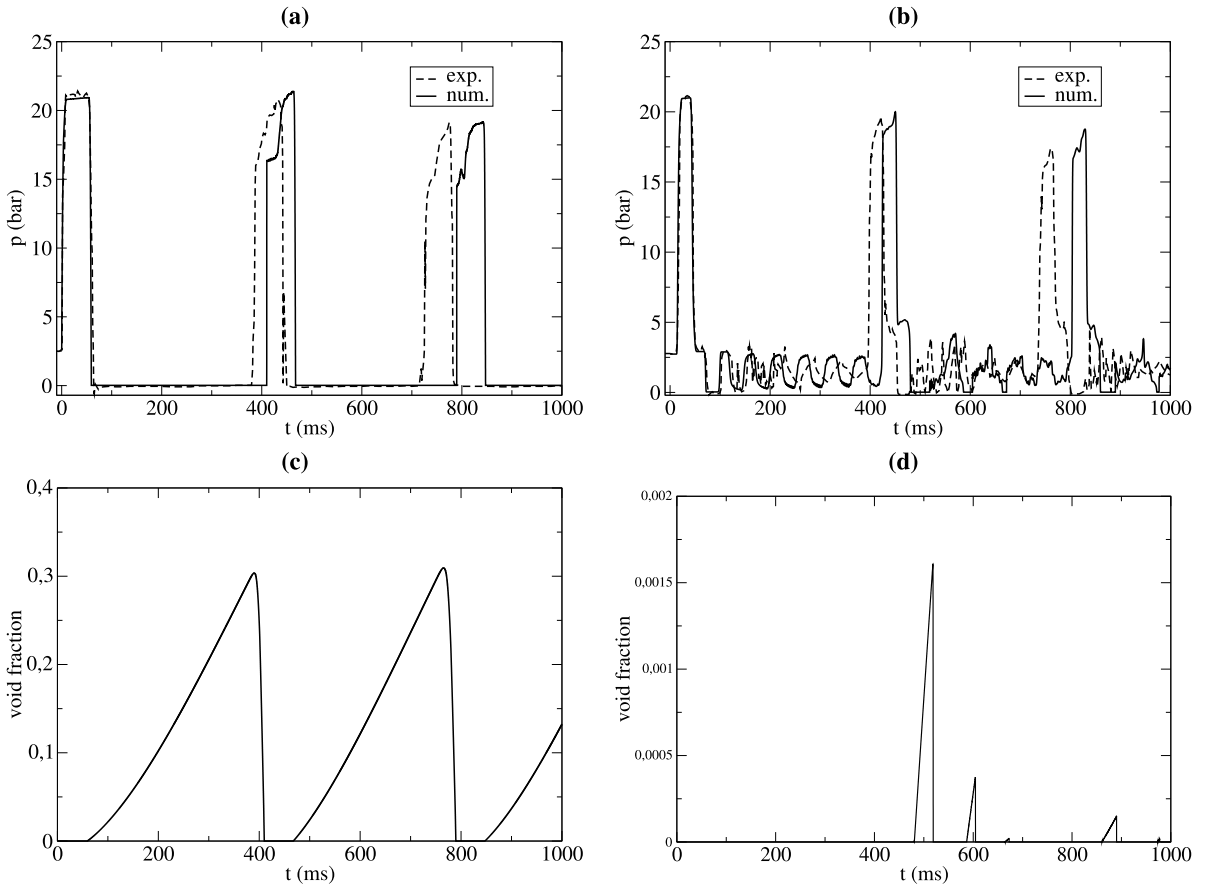


**Fig. 10.** Comparison between numerical solutions obtained with 1000 cells and  $c = 0.8$ ,  $\Delta t = 2 \times 10^{-5}$  s, and the data of Bergant & Simpson's water-hammer experiment with  $u_0 = 1.4 \text{ m s}^{-1}$ : pressure history (a) at  $x = L$  (valve) and (b) at  $x = L/2$ ; void fraction history (c) at  $x = L$  (valve) and (d) at  $x = L/2$ .

#### 4.3.2. Case 2: severe cavitation ( $u_0 = 1.4 \text{ m s}^{-1}$ )

This experimental case corresponds to a water-hammer with severe cavitation. The time evolution of pressure and void fraction at the valve and at the middle of the pipe are plotted in Fig. 10. The correspondence with the experiments is satisfactory for this severely cavitating water-hammer. However the second and third pressure pulse is delayed in the computation. The maximum pressure value at  $t = 0$  ms at the valve corresponds to the Joukowski rise, i.e.  $p = p_0 + \rho_0 \tilde{c}_0 u_0 \approx 21.15$  bar. The duration of each pressure pulse is  $2L/\tilde{c}_0 \approx 57$  ms. Once again, at the valve there is a strong correlation between pressure and void fraction. A 300 times larger cavitation bubble is generated in comparison with the previous case. This test involves large pressures (20 bar), very steep wave fronts (nearly instantaneous) and repetitive behavior (tens of times) which form a large (if not destructive) danger in practical systems. As before, the primary pressure wave is well reproduced whereas the second and third pressure waves are delayed. Once again, the use of an unsteady friction model might improve the pressure history for  $t > 200$  ms.

#### 4.4. UMSICHT column-separation water-hammer experiment

The previous five experiments have been conducted at ambient temperature. In contrast, the present one was performed at a much higher temperature (of about 393 K). The considered test was conducted at Fraunhofer Institute for Environmental, Safety and Energy Technology (UMSICHT) at Oberhausen, Germany (Dudlik et al., 2003, 2008). The experimental set-up consists of a 160 m-long stainless steel pipeline with an internal diameter of  $d = 0.108$  m, two bridges (vertical and vertical/horizontal), a fast closing valve situated 8.7 m from a pump and a pressure tank (see Fig. 11). The transient is initiated by the closure of the valve at  $t = 0$ . As a consequence, a rarefaction wave propagates from the valve to the tank in the flow direction. As the saturation vapor pressure is reached, cavitation occurs. Test n. 307 is considered with the initial conditions given in Table 3 using the absolute pressure, which leads to the following values of initial density, speed of sound and saturation pressure:

$$\rho_0 = \rho^{\text{EOS}}(p_0, T_0) = 943.42 \text{ kg m}^{-3}, \quad c_0 = c^{\text{EOS}}(p_0, T_0) = 1496.38 \text{ m s}^{-1} \quad \text{and} \quad p_{\text{sat}}^{\text{EOS}}(T_0) = 1.968 \text{ bar}$$



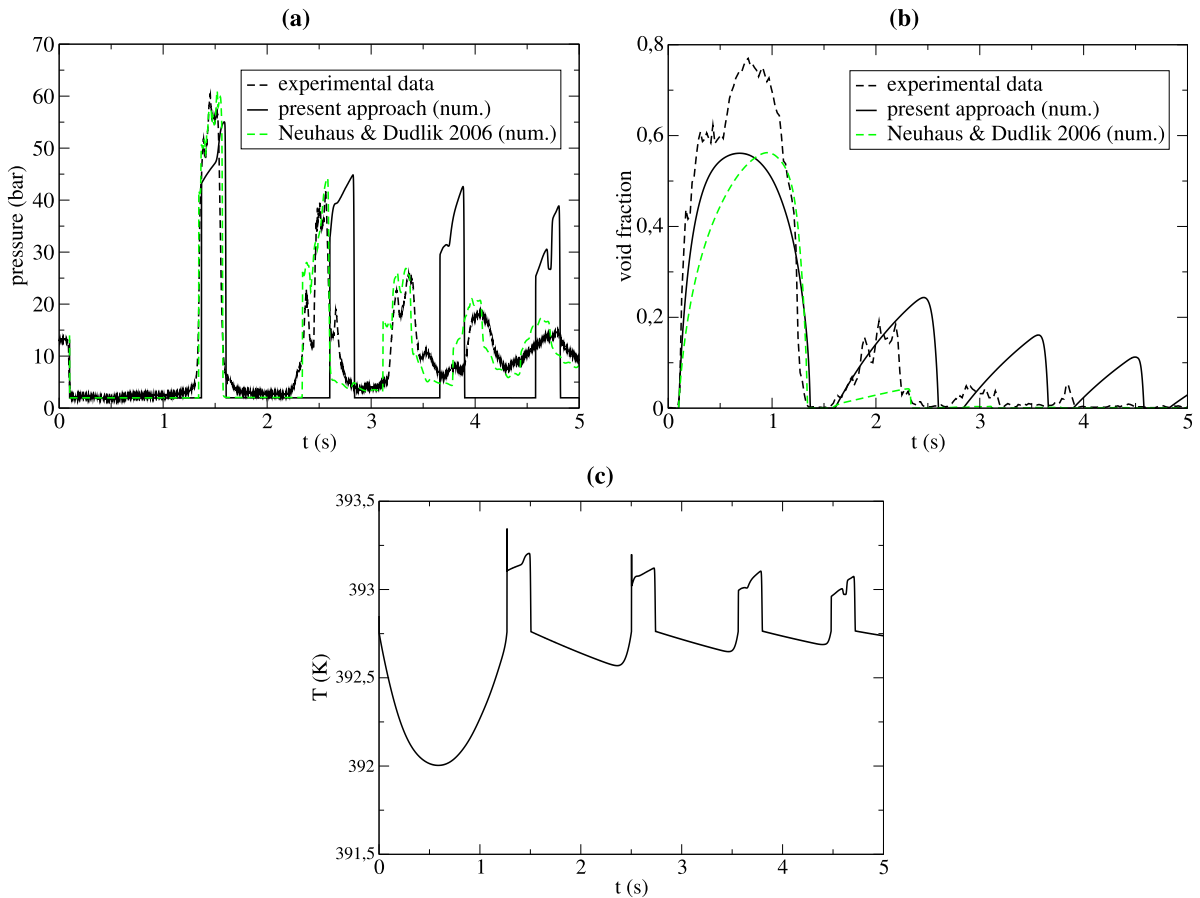


**Fig. 12.** Comparison between numerical solutions obtained with 1000 cells and  $c = 0.8$ ,  $\Delta t = 7.9 \times 10^{-5}$  s, and the data of UMSICHT water-hammer experiment 307: pressure (a); void fraction (b) and temperature (c) histories at P03 (at  $x = 0.2$  m from the valve).

energy equation is taken into account. However, the fluctuation of the temperature is negligible as observed in Fig. 12(c). Finally, Neuhaus and Schaffrath (2012) have shown more recently that, at this high temperature of about 393 K, the effects of thermodynamic non-equilibrium should be considered. These effects are not taken into account in the present simulation as the HEM has been used.

## 5. Conclusion and perspective

A numerical investigation of the water-hammer phenomenon with liquid column-separation due to cavitation is given. The modeling of compressible cavitating flows is based on the Homogeneous Equilibrium Model in conjunction with the 1984 NBS/NRC Steam Tables for steam–water flows. The discretization is obtained using the Finite-Volume approach proposed in Daude and Galon (2018) for solving unsteady compressible flows in pipelines. This FV methodology was previously used for air and water shock-tube problems, and assessed by simulating an experiment on highly nonlinear wave propagation in a liquid-filled pipe (Daude and Galon, 2018). In addition, the present modeling of fast transients also considers skin friction, gravity and non-instantaneous valve closure. Particular attention is paid to the cavitation phenomenon. For this purpose, two theoretical 1-D cavitating Riemann problems are considered. Then water-hammer events with column-separation induced by cavitation are studied. The numerical results are compared with experimental data available in the literature. Good agreement is obtained for the pressure histories along the pipeline without introducing spurious pressure oscillations on fine meshes as in DVCM. The adopted approach makes it possible to compute the generation and the dynamics (growth/collapse) of vapor cavities or bubbles when the absolute pressure reaches the saturation pressure of vapor which cannot be carried out by the classical methods. The nonlinear convective terms, which are significant when the wave speed has become low because of vapor bubbles, are taken into account. In contrast to DVCM and DGCM, the variation of the temperature of the fluid is considered. Finally, the use of conservative equations ensures the correct computation of shocks. On the basis of these results, a numerical study is done on the physical phenomena occurring during column-separation. In particular, it seems that cavitation occurs only in the region near the closed valve because tank pressure prevails at the other end. In a

first phase, the two-phase mixture zone increases in size and then reduces. This leads to a total and sudden disappearance of the vapor which generates a secondary water-hammer. During the propagation of the primary and secondary pressure waves, their interaction leads to a magnitude which can be higher than predicted by the classical Joukowsky formula. Finally, the influence of the initial velocity before valve closure on the size and the duration of the first cavity is examined.

In order to improve the pressure damping during the WH wave propagation unsteady friction modeling should be added to the present approach. Further investigations may concern the dynamic fluid–structure interaction necessary to estimate the vibration of the pipeline system. For example, in realistic pipe systems involving movable bends or knees, the FSI junction coupling has to be considered. In addition, water-hammer can also be generated by the direct contact condensation (DCC) between hot vapor and cold water leading to the so-called condensation-induced water-hammer (CIWH). For this dangerous phenomena, the compressible two-phase counter-current flow with different temperatures should be modeled. In particular, the interphase heat and mass transfer should be taken into account. That is why investigations of the Baer–Nunziato model characterized by two phasic velocities and two phasic temperatures have been undertaken (Crouzet et al., 2015; Lochon et al., 2016, 2017). Finally, ongoing research focuses on the application of the present numerical approach to the rupture of a pressurized pipe in which an expansion wave causes strong hydrodynamic loads.

## Acknowledgments

This work has been achieved within the framework of the “FAST” project of the EDF/CEA/AREVA tripartite institute. Computational facilities were provided by EDF. Numerical simulations have been performed with the *Europlexus* software. The authors gratefully acknowledge Dr. Anton Bergant (Litostroj Power d.o.o., Ljubljana, Slovenia), Prof. Angus Simpson (University of Adelaide, Adelaide, Australia) and Dr. Thorsten Neuhaus (TUEV Nord EnSys GmbH & Co. KG, Hamburg, Germany) for providing the data of their column-separation experiments used to validate the present approach.

## Appendix A. Fluid velocity variation during valve closure for the three Simpson’s water-hammer experiments

The history of the fluid velocity at the valve during valve closure for the three Simpson’s experiments considered herein are reported in Table A.4. The collected data are given in the PhD thesis of Simpson (1986) (see Appendix B pages 181–190). In practice, the imposed fluid velocity  $v(t)$  used in Eq. (12) is obtained using linear interpolations between two successive instants.

## Appendix B. Analysis of the physical phenomena occurring during column-separation

In order to better understand the different phenomena occurring during column-separation, in particular the complex interaction between pressure waves and phase changes, Simpson’s water-hammer experiment with  $u_0 = 0.401 \text{ m s}^{-1}$  and  $p_0 = 3.281 \text{ bar}$  from Section 4.2.2 is considered here again. For simplicity, the analysis is done using a frictionless computation with instantaneous valve closure and without taking into account gravity, i.e.  $f_{DW} = 0$ ,  $\tau(t) = 0$  and  $\theta = 0^\circ$ , leading to the results plotted in Fig. B.13 and compared with the experimental data. Based on this computation, the pressure, velocity and void fraction profiles along the pipe are considered at different instants in Figs. B.14–B.16. At  $t = 0 \text{ s}$ , a pressure wave is generated at the valve due to its sudden closure. The amplitude of this pressure wave can be estimated using the Joukowsky relation:  $p_1 = p_0 + \rho_0 \tilde{c}_0 u_0 \approx 8.334 \text{ bar}$ . The corresponding velocity value is  $u_1 = 0 \text{ m s}^{-1}$ . This pressure wave ( $p_1, u_1$ ) propagates from the valve to the tank (see Step 1 in Fig. B.17) and reaches the tank at  $t = L/\tilde{c}_0 \approx 28.5 \text{ ms}$  (see Fig. B.14-left). Then, the pressure wave is reflected at the tank imposing its constant pressure value, i.e.  $p_2 = p_{\text{tank}} = p_0 = 3.281 \text{ bar}$ . The associated velocity value can be estimated by the Joukowsky relation leading to  $u_2 = u_1 + (p_2 - p_1)/\rho_0 \tilde{c}_0 = -u_0 = -0.401 \text{ m s}^{-1}$ .

Thus, the pressure wave ( $p_2, u_2$ ) propagates from the tank to the valve along the pipe (see Step 2 in Fig. B.17) and reflects at the valve at  $t = 2L/\tilde{c}_0 \approx 57 \text{ ms}$  (see Fig. B.14-right). This reflection leads to a theoretical pressure value below the saturation pressure, i.e.  $p_2 + \rho_0 \tilde{c}_0 u_2 < p_{\text{sat}}$ . As a consequence, the phenomenon of water cavitation occurs at the valve in order to maintain the pressure at the saturation value, i.e.  $p_3 = p_{\text{sat}} \approx 0.03 \text{ bar}$ . The associated velocity jump can be estimated by the Joukowsky relation:  $(\Delta u)_3 = (p_0 - p_{\text{sat}})/\rho_0 \tilde{c}_0 \approx 0.258 \text{ m s}^{-1}$  and the velocity value is  $u_3 = u_2 + (\Delta u)_3 \approx -0.143 \text{ m s}^{-1}$ . We observe in Fig. B.14-right that this value is retrieved correctly in the present computation.

Thus, the pressure wave ( $p_3, u_3$ ) propagates from the valve along the pipe (see Step 3 in Fig. B.17) and reaches the tank at  $t = 3L/\tilde{c}_0 \approx 85.5 \text{ ms}$ . Notice that at  $t = 3L/\tilde{c}_0$ , even if all of the water filling the pipe is at saturation pressure, vapor is only generated in the region near the valve:  $34 \text{ m} \leq x \leq 36 \text{ m}$  (see Fig. B.15-left). At the reflection at the tank, the tank pressure is once again imposed:  $p_4 = p_{\text{tank}} = p_0 = 3.281 \text{ bar}$ . The corresponding velocity is  $u_4 = u_3 + (\Delta u)_3 \approx 0.115 \text{ m s}^{-1}$ .

Thus, the pressure wave ( $p_4, u_4$ ) propagates from the tank to the valve (see Step 4 in Fig. B.17) and should reach the valve at  $t = 4L/\tilde{c}_0 \approx 114 \text{ ms}$ . However, due to the presence of some vapor ahead of the valve, the pressure wave ( $p_4, u_4$ ) never reaches the valve and reflects at the vapor region (see Fig. B.15-right). Notice that there is an abrupt change in speed of sound  $c$  and density  $\rho$  between the liquid single-phase water and the two-phase mixture (at saturation). The corresponding reflection  $C_{\mathcal{R}}$  and transmission  $C_{\mathcal{T}}$  coefficients are given (Rienstra and Hirschberg, 2016) by  $C_{\mathcal{R}} = \frac{\rho_l c_l - \rho_m c_m}{\rho_l c_l + \rho_m c_m}$  and  $C_{\mathcal{T}} = \frac{2\rho_m c_m}{\rho_l c_l + \rho_m c_m}$ . Due to the high difference of acoustic impedance  $\rho c$  between the region where water is in single liquid-phase and the two-phase

**Table A.4**

Fluid velocity variation during the valve closure from (Simpson, 1986) (a)  $u_0 = 0.239 \text{ m s}^{-1}$  (with  $t_0 = -19 \text{ ms}$ ); (b)  $u_0 = 0.401 \text{ m s}^{-1}$  (with  $t_0 = -14 \text{ ms}$ ) and (c)  $u_0 = 1.125 \text{ m s}^{-1}$  (with  $t_0 = -34 \text{ ms}$ ). Time  $t_0$  corresponds to the physical time associated to the beginning of the computation.

(a)		(b)		(c)	
Time (ms)	Velocity ( $\text{m s}^{-1}$ )	Time (ms)	Velocity ( $\text{m s}^{-1}$ )	Time (ms)	Velocity ( $\text{m s}^{-1}$ )
00.00	0.2390	00.00	0.4010	00.00	1.1250
00.88	0.2392	00.88	0.3977	00.88	1.1255
06.15	0.2392	01.60	0.3956	01.76	1.1249
07.03	0.2391	02.64	0.3935	02.64	1.1249
07.91	0.2371	03.52	0.3927	03.52	1.1261
08.79	0.2369	04.39	0.3908	04.39	1.1264
11.43	0.2369	05.27	0.3867	05.27	1.1256
12.30	0.2361	06.15	0.3818	06.15	1.1269
14.06	0.2320	07.03	0.3735	07.03	1.1248
14.94	0.2299	07.91	0.3651	07.91	1.1206
15.82	0.2278	08.79	0.3531	08.79	1.1221
16.70	0.2241	09.67	0.3343	09.67	1.1226
17.58	0.2185	10.55	0.3083	10.55	1.1213
18.46	0.2112	11.43	0.2741	11.43	1.1202
19.34	0.2005	12.30	0.2324	15.82	1.1202
20.21	0.1854	13.18	0.1827	16.70	1.1152
21.09	0.1681	14.06	0.1185	17.58	1.1131
21.97	0.1452	14.94	0.0582	18.46	1.1120
22.85	0.1162	15.82	0.0115	19.34	1.1100
23.73	0.0802	16.70	0.0005	20.21	1.1074
24.61	0.0456	17.58	0.0000	21.09	1.1032
25.49	0.0204			21.97	1.0991
26.37	0.0077			22.85	1.0909
27.25	0.0042			23.73	1.0809
28.13	0.0022			24.61	1.0676
29.00	0.0000			25.49	1.0542
				26.37	1.0374
				27.25	1.0134
				28.13	0.9852
				29.00	0.9498
				29.88	0.9000
				30.76	0.8447
				31.64	0.7659
				32.52	0.6749
				33.40	0.5767
				34.28	0.4703
				35.16	0.3566
				36.03	0.2363
				36.91	0.1200
				37.79	0.0470
				38.67	0.0168
				39.55	0.0062
				40.43	0.0024
				41.31	0.0013
				42.19	0.0012
				43.07	0.0000

mixture (at saturation) region, we obtain  $C_{\mathcal{R}} \approx 1$  and  $C_{\mathcal{T}} \approx 0$ . As a consequence, we assume that the vapor pocket imposes its pressure, i.e.  $p_5 = p_{\text{sat}} \approx 0.03 \text{ bar}$ . The corresponding velocity value is  $u_5 = u_4 + (\Delta u)_3 \approx 0.373 \text{ m s}^{-1}$ .

The profiles near the valve given in Fig. B.16-left show that in the wake of the pressure wave ( $p_5, u_5$ ), which has reflected at the two-phase mixture zone, some pressure and velocity oscillations occur. During the propagation of the pressure wave ( $p_5, u_5$ ) from the valve to the tank (see Step 5 in Fig. B.17), the two-phase mixture zone contracts due to the difference between the external and the internal pressures (see Fig. B.16-right). This leads to the total disappearance of the two-phase mixture, i.e. the collapse of the vapor pocket. According to Wylie et al. (1993), the duration of cavity  $T_v$  can be estimated using the following relation:

$$T_v = \frac{2L}{\tilde{c}_0} \frac{\rho_0 \tilde{c}_0 u_0}{p_0 - p_{\text{sat}}} \quad (\text{B.1})$$

Using this relation, the theoretical instant of collapse denoted here by  $\tau_0^{\text{th}}$  is given by:  $\tau_0^{\text{th}} = 2L/\tilde{c}_0 + T_v \approx 145.5 \text{ ms}$ . The numerical computation gives  $t = \tau_0 \approx 135 \text{ ms}$  which corresponds to a difference of 8%. In the same way, the rate of growth of the first void denoted by  $u_v$  can be estimated by  $-u_3$ , i.e. the flow velocity after the wave reflection leading to the

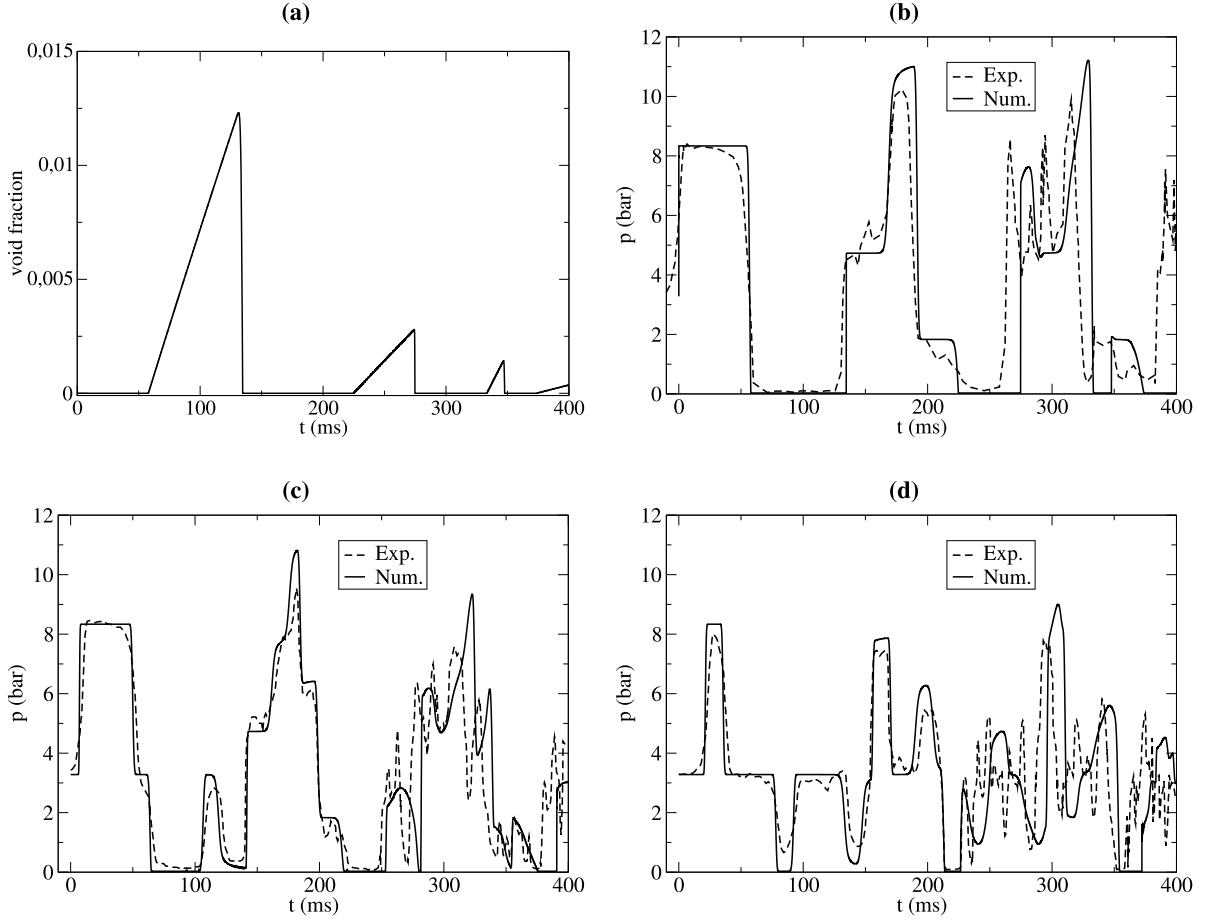


**Fig. B.13.** Comparison between numerical solutions obtained with  $f_{DW} = 0$ ,  $\theta = 0^\circ$  and  $t_c = 0$  using 1000 cells and  $c = 0.8$ ,  $\Delta t = 1.92 \times 10^{-5}$  s, and the data of Simpson's water-hammer experiment with  $u_0 = 0.401$  m s $^{-1}$ : void fraction history (a) at  $x = L$  (valve); pressure history (b) at  $x = L$  (valve); (c) at  $x = 3L/4$ ; (d) at  $x = L/4$ .

saturation pressure:

$$u_v = -u_3 \quad \left( = u_0 - \frac{p_0 - p_{\text{sat}}}{\rho_0 \tilde{c}_0} \right) \quad (\text{B.2})$$

At the vapor collapse, the velocity of the water which impacts the valve is  $u_5$  leading to the Joukowski pressure  $p_6 = p_5 + \rho_0 \tilde{c}_0 u_5 \approx 4.73$  bar retrieved in the computation. The associated closed-valve velocity is  $u_6 = 0$  m s $^{-1}$  (see Fig. B.16-right).

Thus, the pressure wave ( $p_6$ ,  $u_6$ ) is generated at  $t = \mathcal{T}_0 \approx 135$  ms at the valve and propagates towards the tank (see Step 6 in Fig. B.18). Two pressure waves ( $p_5$ ,  $u_5$ ) and ( $p_6$ ,  $u_6$ ) propagate now along the pipe to the tank. The pressure wave ( $p_5$ ,  $u_5$ ) reflects at  $t = 5L/\tilde{c}_0 \approx 142.5$  ms at the tank which imposes its own pressure leading to the pressure  $p_7 = p_{\text{tank}} = p_0 = 3.281$  bar and the velocity  $u_7 = u_5 + (\Delta u)_3 \approx 0.631$  m s $^{-1}$ .

The pressure wave ( $p_7$ ,  $u_7$ ) propagates towards the valve whereas the pressure wave ( $p_6$ ,  $u_6$ ) propagates towards the tank (see Step 7 in Fig. B.18). These two pressure waves start interacting at  $t = t_1 \approx 5L/\tilde{c}_0 + \mathcal{T}_0/2 - 2L/\tilde{c}_0 \approx 153$  ms resulting in the following magnitudes:  $p_8 = p_5 + (p_7 - p_5) + (p_6 - p_5) \approx 7.98$  bar and  $u_8 = u_5 + (u_7 - u_5) + (u_6 - u_5) = (\Delta u)_3 \approx 0.258$  m s $^{-1}$  (see Step 8 in Fig. B.18). Then, the pressure wave ( $p_8$ ,  $u_8$ ) reaches the tank and reflects at  $t = \mathcal{T}_0 + L/\tilde{c}_0 \approx 163.5$  ms leading to the pressure and velocity levels:  $p_9 = p_0$  (tank condition) and thus  $u_9 = -u_5 + (\Delta u)_3 = u_0 - 2(\Delta u)_3 \approx -0.115$  m s $^{-1}$  (according to the Joukowski relation). Afterwards, the pressure ( $p_8$ ,  $u_8$ ) reaches the valve and reflects at  $t = 6L/\tilde{c}_0 \approx 171$  ms leading to the magnitude:  $p_{10} = p_8 + \rho_0 \tilde{c}_0 u_8 \approx 11.23$  bar and  $u_{10} = 0$  m s $^{-1}$ . Note that this pressure level is higher than the initial Joukowski rise of 8.334 bar.

The pressure wave ( $p_{10}$ ,  $u_{10}$ ) propagates towards the tank whereas the wave ( $p_9$ ,  $u_9$ ) propagates towards the valve (see Step 9 in Fig. B.18). As a consequence, these two waves interact at  $t = t_2 \approx 7L/\tilde{c}_0 + \mathcal{T}_0/2 - 2L/\tilde{c}_0 \approx 181.5$  ms leading to the following pressure and velocity levels:  $p_{11} = p_8 + (p_9 - p_8) + (p_{10} - p_8) = 2p_0 - p_{\text{sat}} \approx 6.532$  bar and  $u_{11} = u_8 + (u_9 - u_8) + (u_{10} - u_8) = u_0 - 3(\Delta u)_3 \approx -0.373$  m s $^{-1}$  (see Step 10 in Fig. B.18).

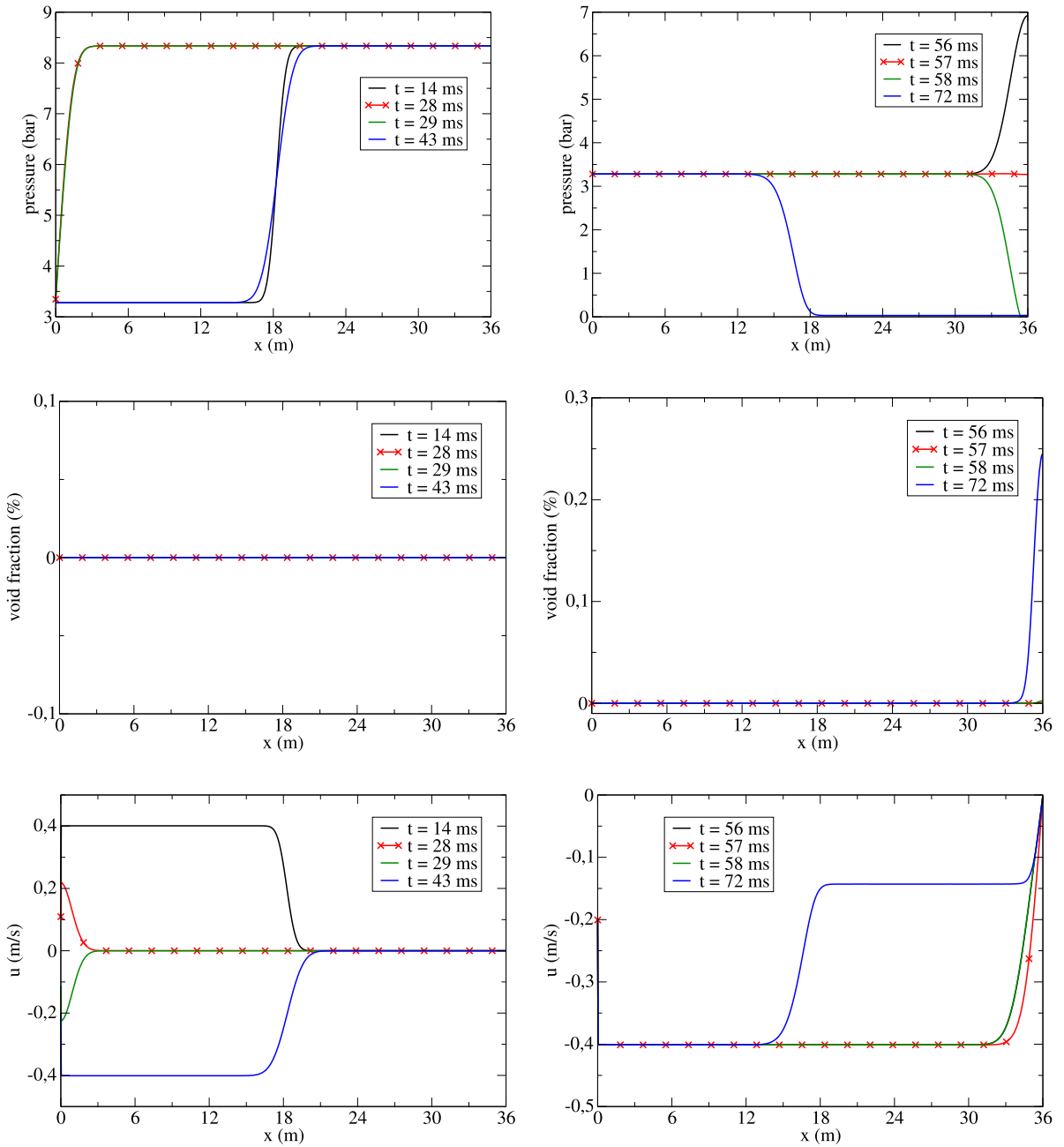


**Fig. B.14.** Pressure (top), void fraction (middle) and velocity (bottom) profiles along the pipe (locations  $x = 0$  m and  $x = 36$  m correspond to the position of the tank and the valve, respectively) at different instants: for  $0 \leq t \leq 3L/\tilde{c}_0$  (left) and  $3L/\tilde{c}_0 \leq t \leq 5L/\tilde{c}_0$  (right).

At  $t = \mathcal{T}_0 + 2L/\tilde{c}_0 \approx 192$  ms, the pressure wave  $(p_{11}, u_{11})$  reaches the valve and reflects leading to the pressure  $p_{12} = p_{11} + \rho_0 \tilde{c}_0 u_{11} \approx 1.83$  bar with  $u_{12} = 0$  m s<sup>-1</sup>. In addition, at  $t = 7L/\tilde{c}_0 \approx 199.5$  ms, the pressure wave  $(p_{11}, u_{11})$  reaches the tank and reflects with  $p_{13} = p_0$  and  $u_{13} = u_0 - 4(\Delta u)_3 \approx -0.631$  m s<sup>-1</sup> (see Step 11 in Fig. B.19). Afterwards, the pressure waves  $(p_{12}, u_{12})$  and  $(p_{13}, u_{13})$  propagating towards the tank and the valve, respectively, interact at  $t = t_{i_3} \approx 8L/\tilde{c}_0 + \mathcal{T}_0/2 - 2L/\tilde{c}_0 \approx 210$  ms. The theoretical pressure due to this interaction is  $p_{th} = p_{11} + (p_{12} - p_{11}) + (p_{13} - p_{11})$  which is well below the saturation pressure, thus cavitation occurs once more leading to the pressure level  $p_{14} = p_{sat}$ . The corresponding velocity is:  $u_{14} = u_{th} + (p_{th} - p_{sat})/(\rho_0 \tilde{c}_0)$  with  $u_{th} = u_{11} + (u_{12} - u_{11}) + (u_{13} - u_{11}) = -(\Delta u)_3$ , thus  $u_{14} \approx -0.373$  m s<sup>-1</sup> (see Step 12 in Fig. B.19).

At  $t = \mathcal{T}_0 + 3L/\tilde{c}_0 \approx 220.5$  ms, the pressure wave  $(p_{14}, u_{14})$  reaches the tank and reflects with  $p_{15} = p_0$  and  $u_{15} = u_{14} + (\Delta u)_3 = -0.115$  m s<sup>-1</sup>. Then, at  $t = 8L/\tilde{c}_0 \approx 228$  ms, the pressure wave  $(p_{14}, u_{14})$  reaches the valve and reflects

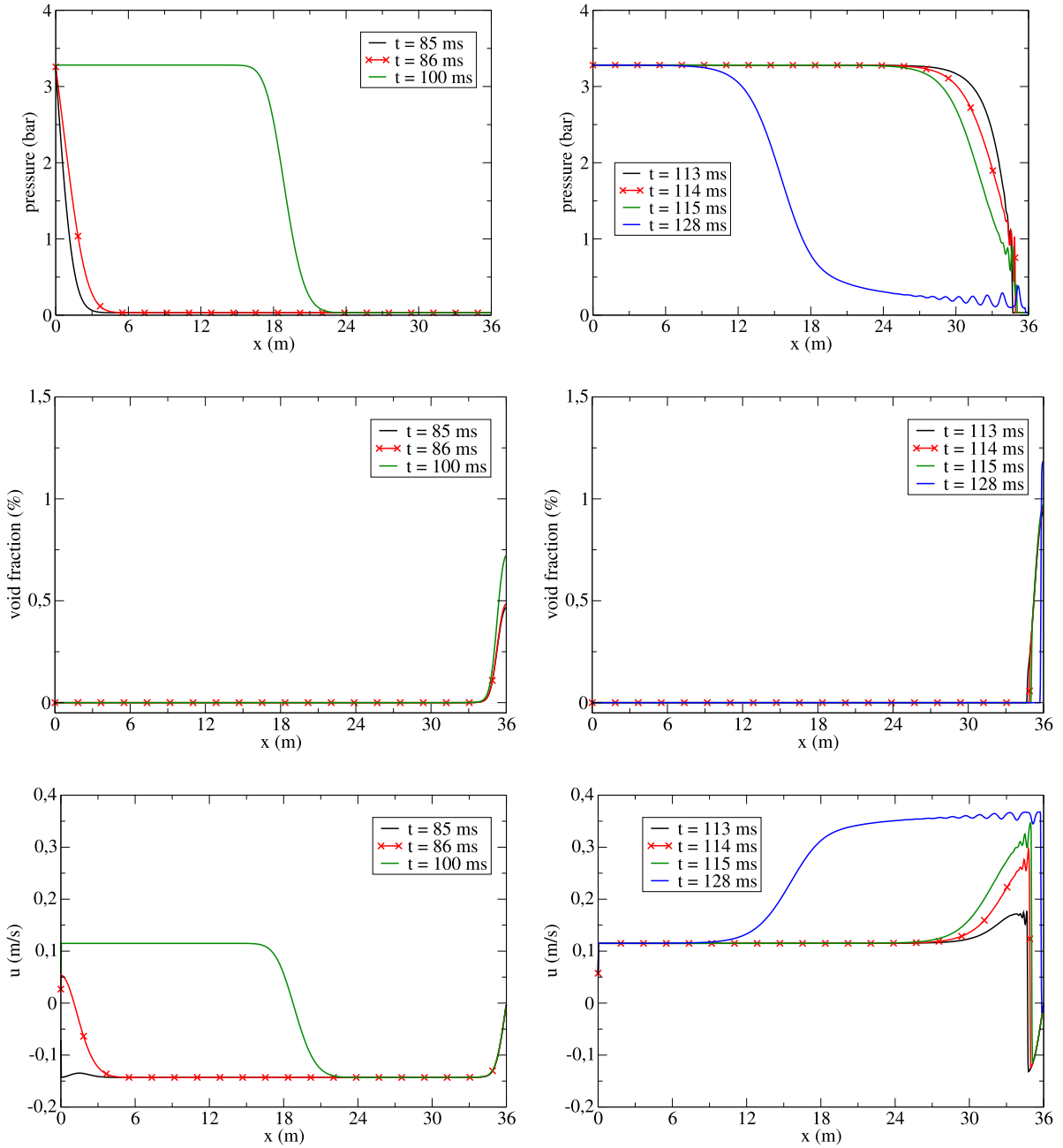


**Fig. B.15.** Pressure (top), void fraction (middle) and velocity (bottom) profiles along the pipe (locations  $x = 0$  m and  $x = 36$  m correspond to the position of the tank and the valve, respectively) at different instants: for  $3L/\tilde{c}_0 \leq t \leq 7L/2\tilde{c}_0$  (left) and  $7L/2\tilde{c}_0 \leq t \leq 9L/2\tilde{c}_0$  (right).

with:  $p = p_{14} + \rho_0 \tilde{c}_0 u_{14}$  which is below the saturation value. Once again cavitation occurs at the valve leading to a new cycle of liquid column-separation. As a consequence, the pressure wave is identified by  $p_{16} = p_{\text{sat}}$  and  $u_{16} = u_{14} \approx -0.373 \text{ m s}^{-1}$  (see Step 13 in Fig. B.19).

The time evolution of the pressure at the valve plotted in Fig. B.13(b) is in full agreement with the quasi-theoretical results described above: for  $0 \leq t \leq 2L/\tilde{c}_0$ ,  $p = p_1 \approx 8.334$  bar; then for  $2L/\tilde{c}_0 \leq t \leq \mathcal{T}_0$ ,  $p = p_{\text{sat}}$ ; then for  $\mathcal{T}_0 \leq t \leq 6L/\tilde{c}_0$ ,  $p = p_6 \approx 4.73$  bar; afterwards for  $6L/\tilde{c}_0 \leq t \leq \mathcal{T}_0 + 2L/\tilde{c}_0$ ,  $p = p_{10} \approx 11.23$  bar; then for  $\mathcal{T}_0 + 2L/\tilde{c}_0 \leq t \leq 8L/\tilde{c}_0$ ,  $p = p_{12} \approx 1.83$  bar; and at  $t = 8L/\tilde{c}_0$ ,  $p = p_{\text{sat}}$  again, leading to the second cavity.

To check the agreement between the quasi-theoretical results and the present numerical simulation, the histories of pressure at  $x = 3L/4$  (plotted in Fig. B.13(c)) and velocity at  $x = L/4$  plotted in Fig. B.20(a) are examined. For the pressure, the different values attained at  $x = 3L/4$  are:  $p_0 = 3.281$  bar; then  $p_1 \approx 8.334$  bar; then  $p_2 = p_0 = 3.281$  bar; then

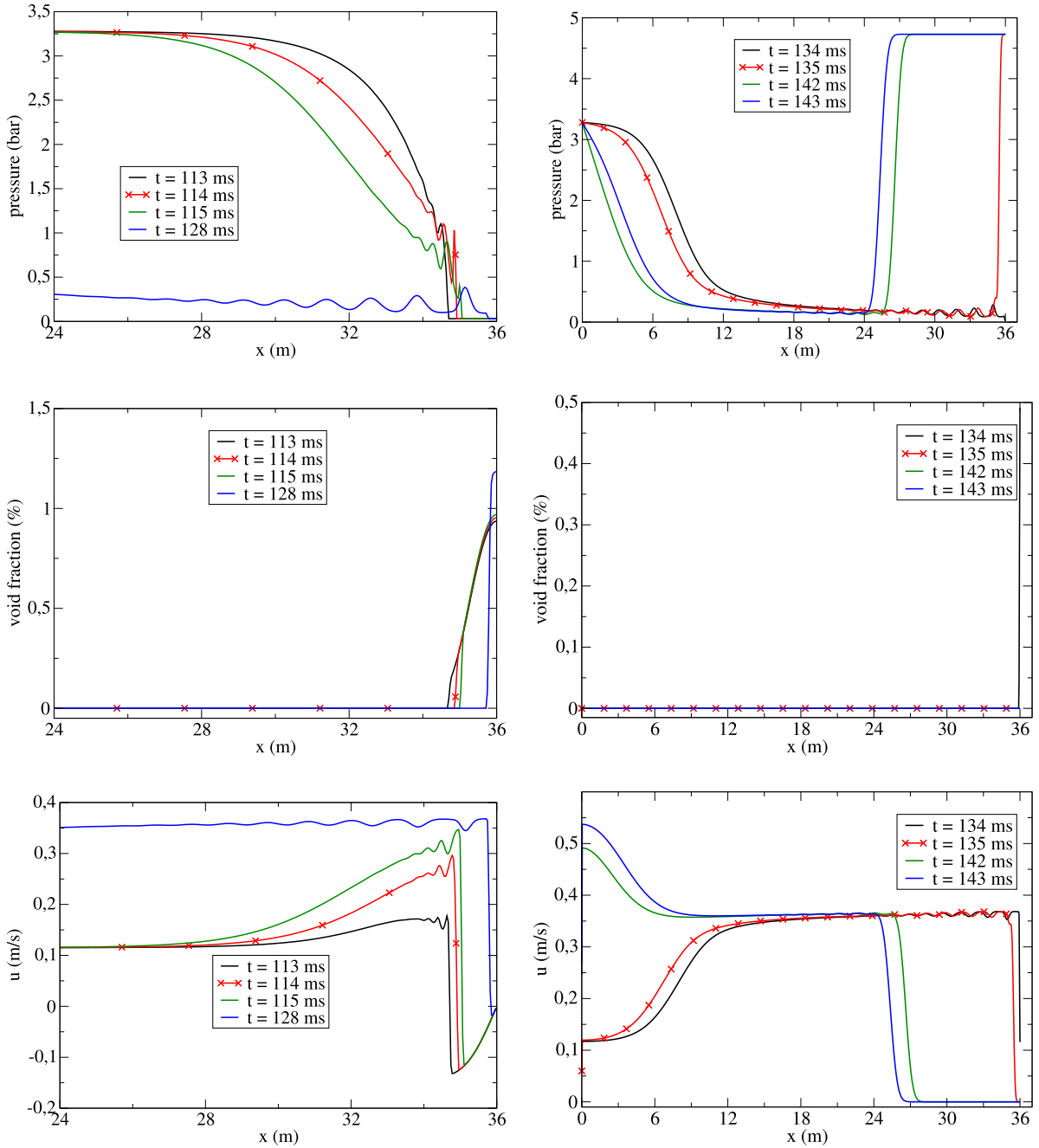


**Fig. B.16.** Pressure (top), void fraction (middle) and velocity (bottom) profiles along the pipe (locations  $x = 0$  m and  $x = 36$  m correspond to the position of the tank and the valve, respectively) at different instants: for  $7L/2\bar{c}_0 \leq t \leq 9L/2\bar{c}_0$ , zoom near the valve (left) and  $9L/2\bar{c}_0 \leq t \leq 11L/2\bar{c}_0$  (right).

$p_3 = p_{\text{sat}}$ ; then  $p_4 = p_0 = 3.281$  bar; then  $p_5 = p_{\text{sat}}$ ; then  $p_6 \approx 4.73$  bar; then  $p_8 \approx 7.98$  bar; then  $p_{10} \approx 11.23$  bar; then  $p_{11} \approx 6.532$  bar; then  $p_{12} \approx 1.83$  bar and finally  $p_{\text{sat}}$  which corresponds to the first 12 pressure levels in the time evolution plotted in Fig. B.13(c).

In the same way, the different values reached by the velocity at  $x = L/4$  (see Fig. B.20(a)) are:  $u_0 = 0.401$  m s<sup>-1</sup>; then  $u_1 = 0$  m s<sup>-1</sup>; then  $u_2 = -0.401$  m s<sup>-1</sup>; then  $u_3 \approx -0.143$  m s<sup>-1</sup>; then  $u_4 \approx 0.115$  m s<sup>-1</sup>; then  $u_5 \approx 0.373$  m s<sup>-1</sup>; then  $u_7 \approx 0.631$  m s<sup>-1</sup>; then  $u_8 \approx 0.258$  m s<sup>-1</sup>; then  $u_9 \approx -0.115$  m s<sup>-1</sup>; then  $u_{11} \approx -0.373$  m s<sup>-1</sup>; then  $u_{13} = -0.631$  m s<sup>-1</sup> and  $u_{14} = -0.373$  m s<sup>-1</sup> which corresponds to the first 12 plateaus of velocity plotted in Fig. B.20(a).

The computed velocity at the tank displayed in Fig. B.20(b) is also in full agreement with the quasi-theoretical results previously described: for  $0 \leq t \leq L/\bar{c}_0$ ,  $u = u_0 = 0.401$  m s<sup>-1</sup>; for  $L/\bar{c}_0 \leq t \leq 3L/\bar{c}_0$ ,  $u = -u_0 = -0.401$  m s<sup>-1</sup>; for

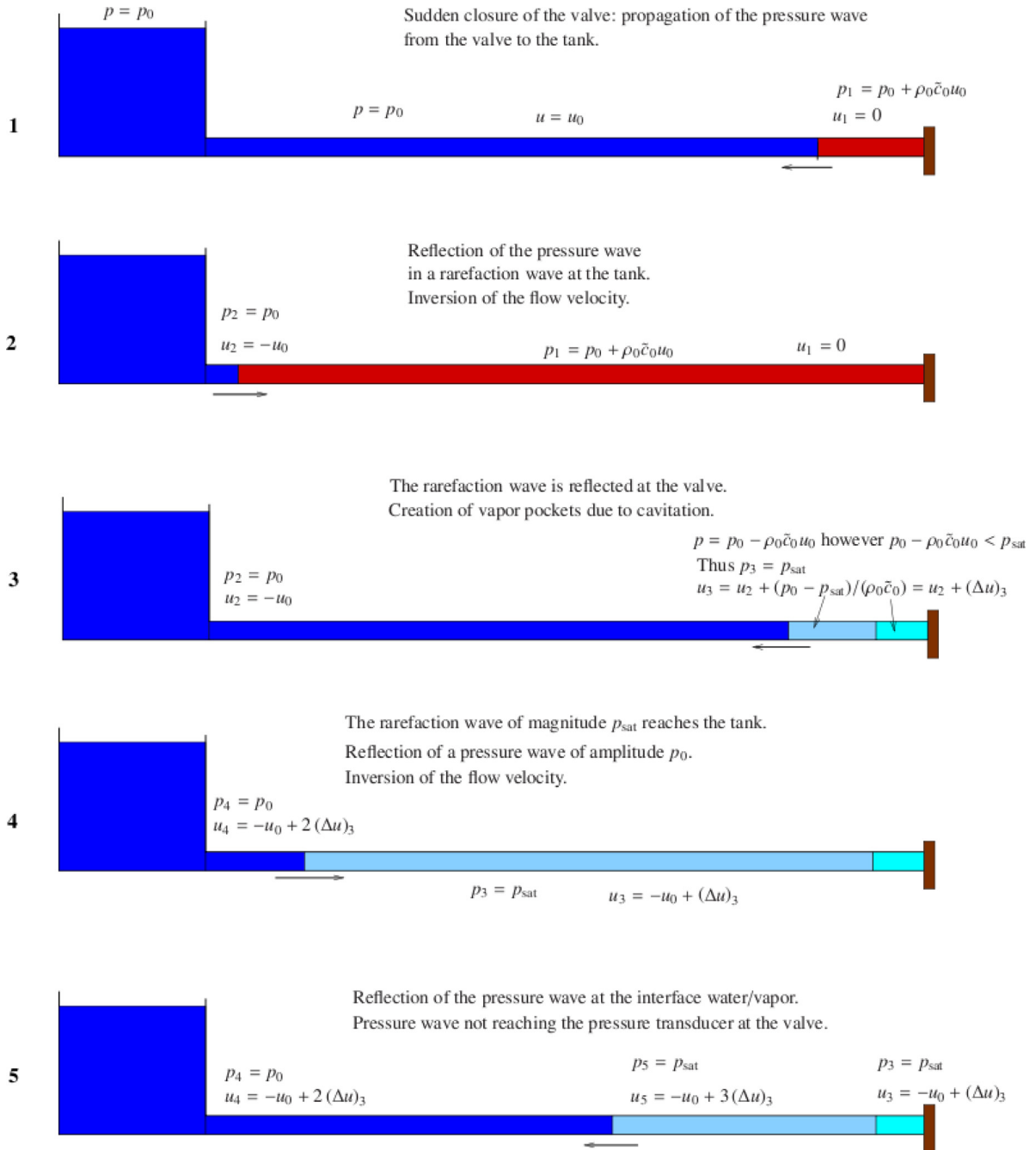


**Fig. B.17.** Propagation of the pressure waves generated during a water-hammer event with column-separation at different instants: 1: for  $0 \leq t < L/\tilde{c}_0$ ; 2: for  $L/\tilde{c}_0 \leq t < 2L/\tilde{c}_0$ ; 3: for  $2L/\tilde{c}_0 \leq t < 3L/\tilde{c}_0$ ; 4: for  $3L/\tilde{c}_0 \leq t < 4L/\tilde{c}_0$ ; 5: for  $4L/\tilde{c}_0 \leq t < \tau_0 \approx 135$  ms.

$3L/\tilde{c}_0 \leq t \leq 5L/\tilde{c}_0$ ,  $u = u_4 \approx 0.115 \text{ m s}^{-1}$ ; for  $5L/\tilde{c}_0 \leq t \leq \tau_0 + L/\tilde{c}_0$ ,  $u = u_7 \approx 0.631 \text{ m s}^{-1}$ ; for  $\tau_0 + L/\tilde{c}_0 \leq t \leq 7L/\tilde{c}_0$ ,  $u = u_9 \approx -0.115 \text{ m s}^{-1}$ ; for  $7L/\tilde{c}_0 \leq t \leq \tau_0 + 3L/\tilde{c}_0$ ,  $u = u_{13} \approx -0.631 \text{ m s}^{-1}$ .

**Appendix C. Influence of the initial flow velocity on the duration of the first vapor cavity**

Fig. C.21 shows the calculated void fractions and pressure histories (using the dimensionless time  $t^* = t\tilde{c}_0/L$ ) near the valve at  $x = L$  and the velocity history at  $x = L/4$  for the three experiments of Simpson considered herein. The calculations

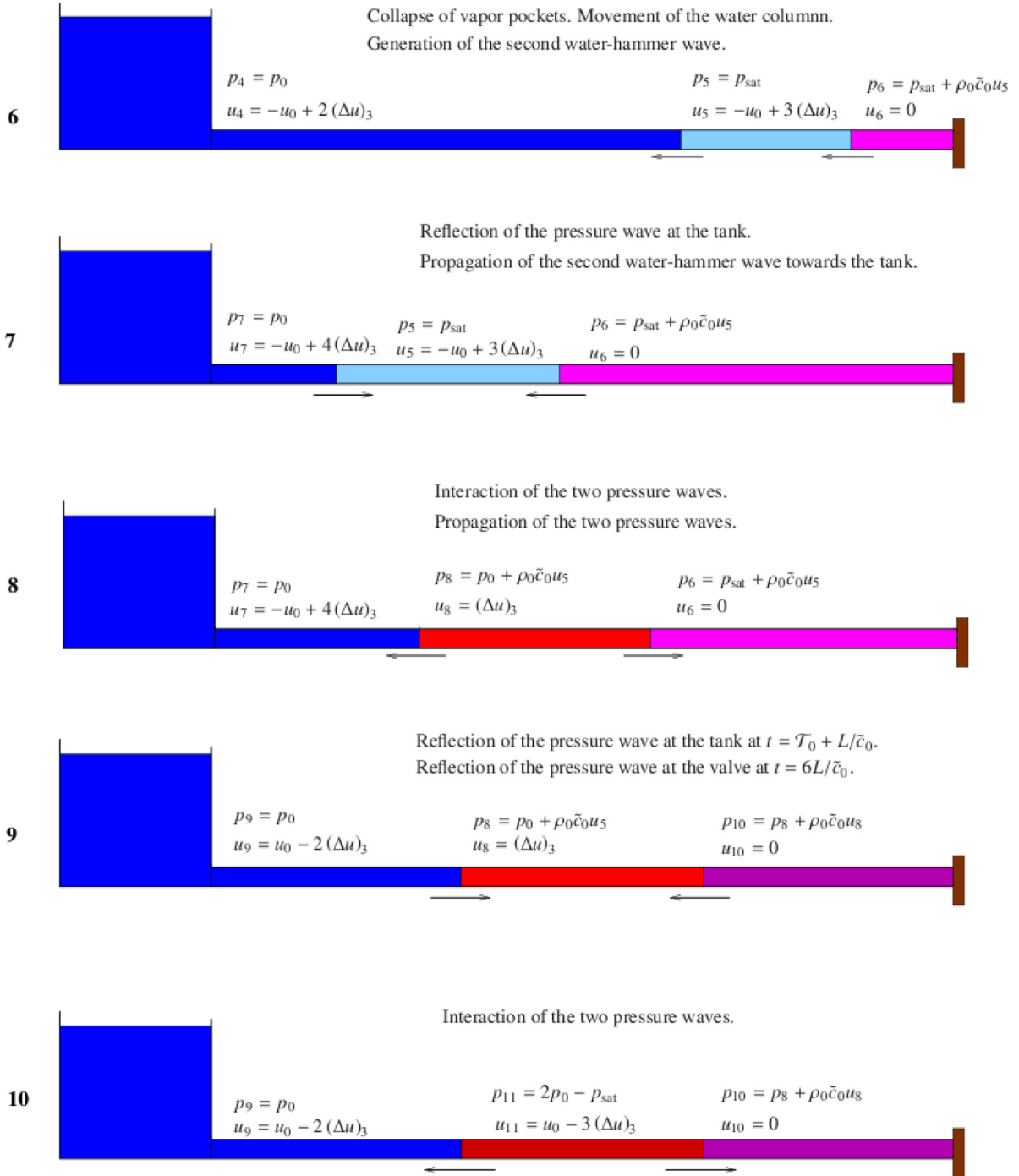


**Fig. B.18.** Propagation of the pressure waves generated during a water-hammer event with column-separation at different instants: 6: for  $135 \text{ ms} \approx \mathcal{T}_0 \leq t < 5L/\tilde{c}_0$ ; 7: for  $5L/\tilde{c}_0 \leq t < t_1$ ; 8: for  $t_1 \leq t < \mathcal{T}_0 + L/\tilde{c}_0$ ; 9: for  $6L/\tilde{c}_0 \leq t < t_2$ ; 10: for  $t_2 \leq t < \mathcal{T}_0 + 2L/\tilde{c}_0$ .

are with instantaneous valve closures and without friction and gravity to simplify the physical behavior. The length of the cavitation phase, the rate of vapor generation and the amount of generated vapor strongly depend on the initial flow velocity.

As discussed before, the duration  $T_v$  of the first cavity can be estimated as derived in Wylie et al. (1993) using Eq. (B.1) leading to the theoretical time of collapse  $\mathcal{T}_0^{\text{th}} = 2L/\tilde{c}_0 + T_v$ . For cavitating flow cases, as discussed in Appendix B, at  $t = 2L/\tilde{c}_0$ , the wave  $(p_{\text{sat}}, -u_0 + (p_0 - p_{\text{sat}})/(\rho_0 \tilde{c}_0))$  is generated at the valve and propagates towards the tank. Then, during the cavitation

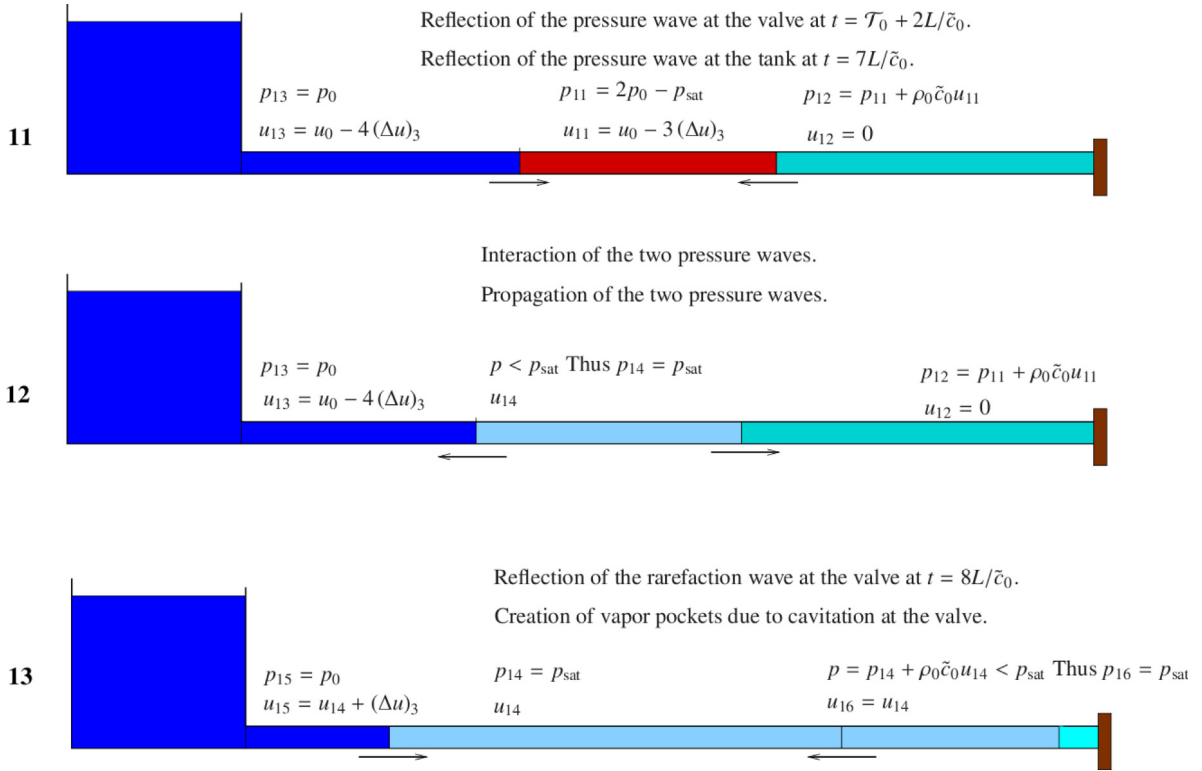


**Fig. B.19.** Propagation of the pressure waves generated during a water-hammer event with column-separation for different instants: 11: for  $7L/\tilde{c}_0 \leq t < t_3$ ; 12: for  $t_3 \leq t < \mathcal{T}_0 + 3L/\tilde{c}_0$ ; 13: for  $8L/\tilde{c}_0 \leq t < t_4$ .

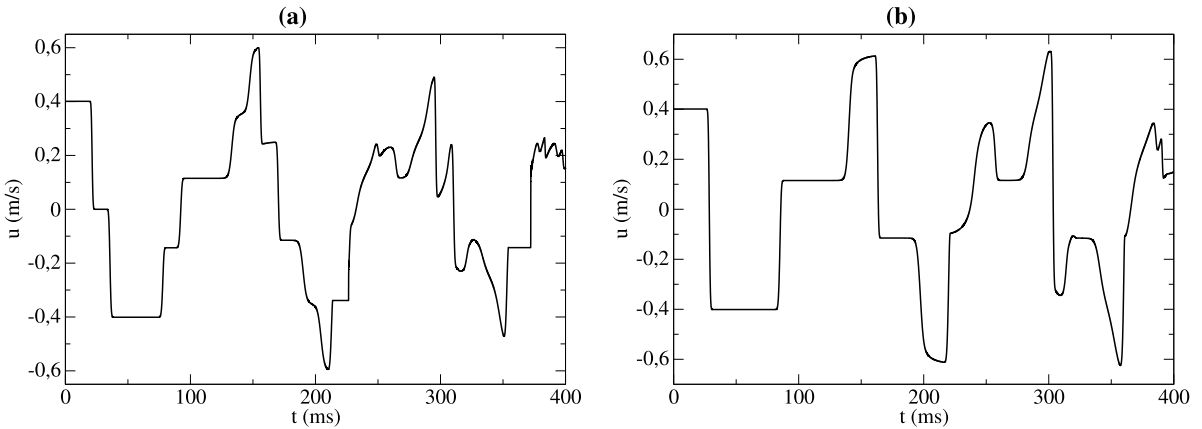


**Fig. B.20.** Numerical solutions obtained with 1000 cells and  $c = 0.8$ ,  $\Delta t = 1.92 \times 10^{-5}$  s, for Simpson's water-hammer experiment with  $u_0 = 0.401$  m s<sup>-1</sup>: velocity history (a) at  $x = L/4$  and (b) at  $x = 0$  (tank).

period, i.e. for  $2L/\tilde{c}_0 \leq t \leq 2L/\tilde{c}_0 + T_v$ , the two boundaries of the pipe are at constant pressure:  $p_0$  at the tank and  $p_{\text{sat}}$  at the valve. Note that the pipe length  $L$  is much larger than the maximum cavity length and that the primary pressure wave propagates up and down along the pipe between the two boundaries (tank and valve) each imposing its own pressure. Consequently, at each reflection, the flow velocity, equal to  $-u_0$  at  $t = 2L/\tilde{c}_0$  (at the beginning of the cavitation period), is increased by  $(p_0 - p_{\text{sat}})/(\rho_0 \tilde{c}_0)$ . The number  $N$  of wave reflections during the cavitation period is given by:

$$N = E \left( \frac{T_v}{L/\tilde{c}_0} \right)$$

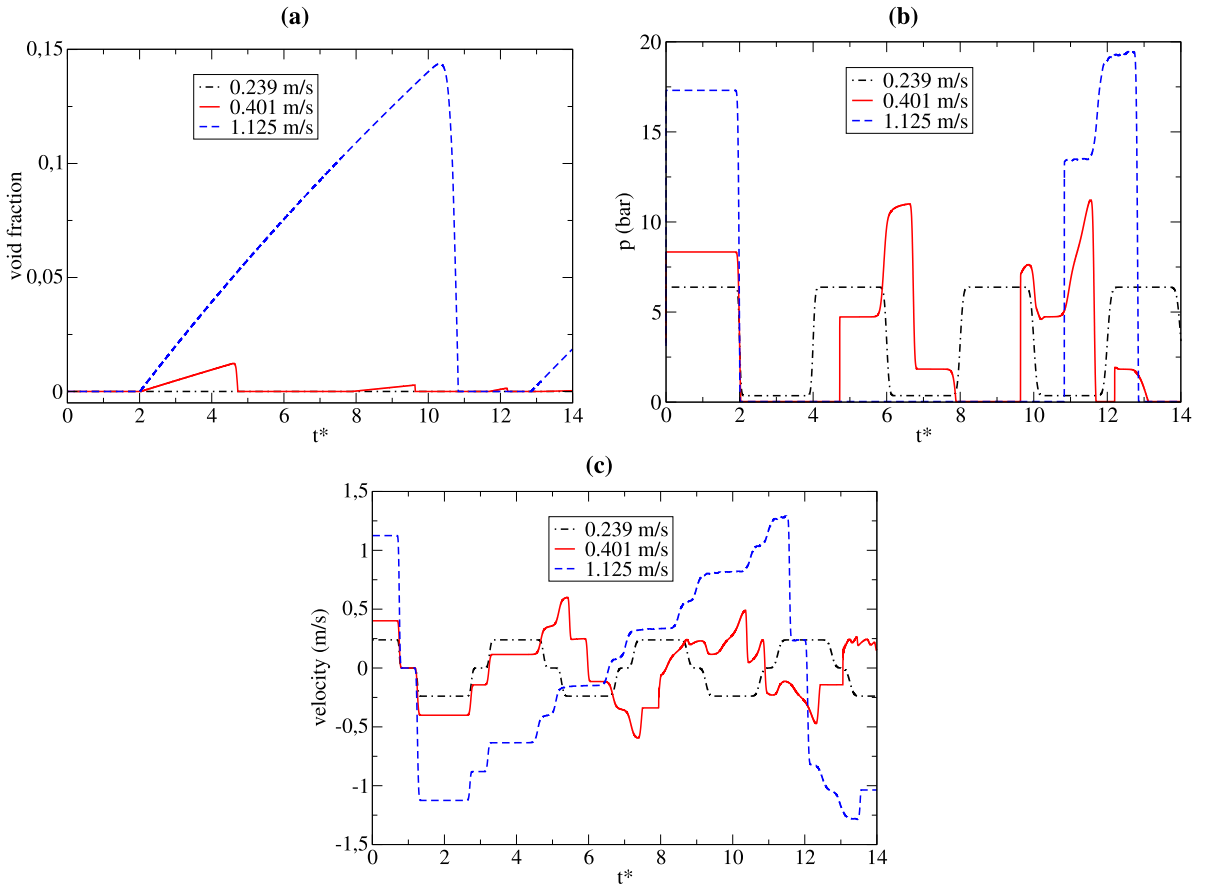


**Fig. C.21.** Numerical solutions obtained with  $f_{DW} = 0$ ,  $\theta = 0^\circ$  and  $t_c = 0$  using 1000 cells and  $c = 0.8$ ,  $\Delta t = 1.92 \times 10^{-5}$  s, of three of Simpson's water-hammer experiments: void fraction history (a); pressure history (b) at  $x = L$  (valve) and velocity history (c) at  $x = L/4$ .

**Table C.5**

Analytical estimations of the pressure magnitude of the secondary water-hammer and its interaction with the primary water-hammer for three of Simpson's column-separation water-hammer experiments compared to numerical results obtained without friction and gravity.

Case	$p_0$ (bar)	$u_0$ (m s <sup>-1</sup> )	$T_0^{\text{th}}$ (ms)	$T_v^{\text{th}}$ (ms)	$N^{\text{th}}$	$u_i^{\text{th}}$ (m s <sup>-1</sup> )	$p_i^{\text{th}}$ (bar)	$p_{ii}^{\text{th}}$ (bar)	$p_i^{\text{num}}$ (bar)	$p_{ii}^{\text{num}}$ (bar)
1	3.469	0.239	/	/	/	/	/	/	/	/
2	3.281	0.401	145.5	88.5	3	0.373	<b>4.73</b>	<b>11.23</b>	<b>4.729</b>	<b>11</b>
3	3.118	1.125	318.6	261.6	9	1.08	<b>13.64</b>	<b>19.82</b>	<b>13.45</b>	<b>19.2</b>

with  $E$  the floor operator. Thus, when the vapor void collapses, i.e. at  $t = 2L/\tilde{c}_0 + T_v$ , the water impacts the valve at the flow velocity  $u_i$  given by:  $u_i = -u_0 + N(p_0 - p_{\text{sat}})/(\rho_0\tilde{c}_0)$ . The successive  $N$  jumps of velocity are visible in Fig. C.21(c). The magnitude of the secondary water-hammer is then directly given by:  $p_i = p_{\text{sat}} + \rho_0\tilde{c}_0u_i$ . The primary and secondary water-hammer pressure waves interact as represented in Fig. C.22. The pressure wave generated by this interaction attains the valve leading to the pressure magnitude of:

$$p_{ii} = p_i + p_0 - p_{\text{sat}} + \rho_0\tilde{c}_0 \frac{p_0 - p_{\text{sat}}}{\rho_0\tilde{c}_0} = p_i + 2(p_0 - p_{\text{sat}}) \quad (\text{C.1})$$

Similar relations are presented in Wylie et al. (1993), Bergant et al. (2006), Mostowsky (1929) and Binnie and Thackrah (1951).

The numerical results of the present analytical derivation for the three experiments conducted by Simpson are summarized in Table C.5. Good agreement with the computer simulations is obtained.

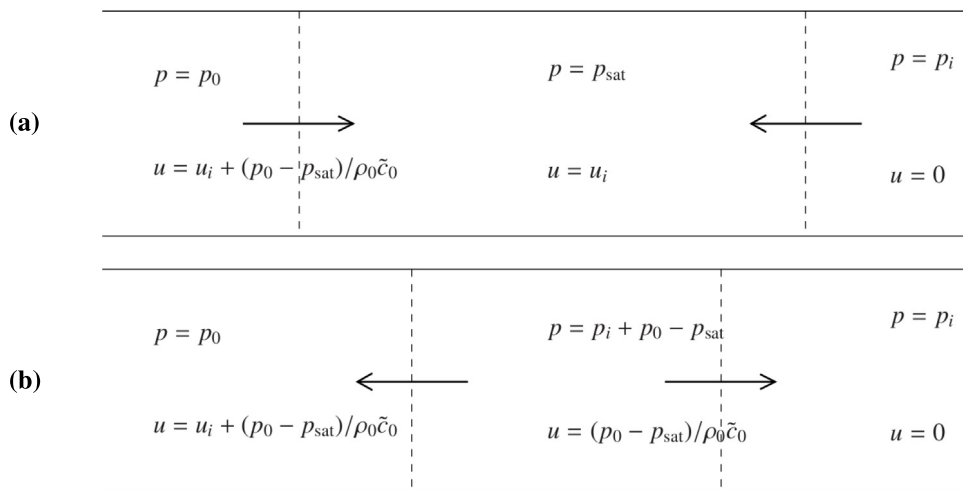


**Fig. C.22.** Representation of the pressure waves interaction between the primary water-hammer due to the sudden valve closure and the secondary water-hammer due to the cavity collapse: before interaction (a) and after interaction (b).

## References

- Allievi, L., 1913. Teoria del colpo d'ariete. Atti del Collegio degli Ingegneri ed Architetti Italiani, Milan, Italy (in Italian) (English translation by E. E. Halmos 1925, The theory of waterhammer, Trans. ASME).
- Bergant, A., Simpson, A.R., 1999. Pipeline column separation flow regimes. ASCE J. Hydraul. Eng. 22 (2), 135–171.
- Bergant, A., Simpson, A.R., Tijsseling, A.S., 2006. Water hammer with column separation: A historical review. J. Fluids Struct. 22 (2), 135–171.
- Bergant, A., Simpson, A.R., Vitovsky, J.P., 2001. Developments in unsteady pipe flow friction modelling. J. Hydraul. Res. 39 (3), 249–257.
- Bergant, A., Tijsseling, A.S., Vitovsky, J.P., Covas, D.I.C., Simpson, A.R., Lambert, M.F., 2008a. Parameters affecting water hammer wave attenuation, shape and timing. Part 1: Mathematical tools. J. Hydraul. Res. 46 (3), 373–381.
- Bergant, A., Tijsseling, A.S., Vitovsky, J.P., Covas, D.I.C., Simpson, A.R., Lambert, M.F., 2008b. Parameters affecting water hammer wave attenuation, shape and timing. Part 2: Case studies. J. Hydraul. Res. 46 (3), 382–391.
- Binnie, A.M., Thackrah, D.G., 1951. Water hammer in a pumping main and its prevention. Proc. Inst. Mech. Eng. 165, 43–52, 65–73.
- Bonin, C.C., 1960. Water hammer damage to Oigawa power station. ASME J. Eng. Power 82 (2), 111–119.
- Bughazem, M.B., Anderson, A., 2000. Investigation of an unsteady friction model for waterhammer and column separation. In: Anderson, A. (Ed.), Proc. of the 8th International Conference on Pressure Surges. The Hague, The Netherlands, pp. 483–498.
- Chaiko, M.A., 2006. A Finite-Volume approach for simulation of liquid-column separation in pipelines. ASME J. Fluids Eng. 128 (6), 1324–1335.
- Chaudhry, M.H., 2014. Applied Hydraulic Transients, third ed. Springer.
- Clerc, S., 2000. Numerical simulation of the homogeneous equilibrium model for two-phase flows. J. Comput. Phys. 161 (1), 354–375.
- Crouzet, F., Daude, F., Galon, P., Hérard, J.-M., Hurisse, O., Liu, Y., 2015. Validation of a two-fluid model on unsteady water-vapour flows. Comput. & Fluids 119, 131–142.
- Daude, F., Galon, P., 2018. A Finite-Volume approach for compressible single- and two-phase flows in flexible pipelines with fluid-structure interaction. J. Comput. Phys. 362 (C), 375–408.
- Dudlik, A., Prasser, H.M., Apostolidis, A., Bergant, A., 2008. Water hammer induced by fast-acting valves: experimental studies at pilot plant pipework. Multiph. Sci. Technol. 20 (3–4), 239–263.
- Dudlik, A., Schönfeld, S.B.H., Hagemann, O., Fahlenkamp, H., 2003. Water hammer and cavitation hammer in process plant pipe systems. Kerntechnik 68 (3), 91–96.
- Dumbser, M., Iben, U., Munz, C.-D., 2013. Efficient implementation of high order unstructured WENO schemes for cavitating flows. Comput. & Fluids 86, 141–168.
- Gale, J., Tiselj, I., 2002. Water hammer in elastic pipes, International Conference on Nuclear Energy for New Europe '02, Kranjska Gora, Slovenia, Sept. 9–12.
- Ghidaoui, M.S., Zhao, M., McInnis, D.A., Axworthy, D.H., 2005. A review of water hammer theory and practice. ASME Appl. Mech. Rev. 58 (1), 49–76.
- Guinot, V., 2000. Riemann solvers for water hammer simulations by Godunov method. Internat. J. Numer. Methods Engrg. 49 (7), 851–870.
- Haar, L., Gallagher, J.S., Kell, G.S., 1984. NBS/NRC Steam Tables: Thermodynamic and Transport Properties and Computer Programs for Vapor and Liquid States of Water in SI Units. Hemisphere Publishing Co.
- Hirsch, C., 1988. Numerical Computation of Internal and External Flows. J. Wiley and Sons, New-York.
- Hwang, Y.-H., Chung, N.-M., 2002. A fast Godunov method for the water-hammer problem. Internat. J. Numer. Methods Fluids 40 (6), 799–819.
- Joint Research Centre (JRC), 2018. Commissariat à l'énergie atomique et aux énergies alternatives (CEA), Europlexus user's manual, <http://europlexus.jrc.ec.europa.eu/>.
- Joukowski, N.E., 1900. Über den hydraulischen Stoss in Wasserleitungsröhren (On the hydraulic hammer in water supply pipes). Mém. Acad. Impériale Sci. St.-Pétersbourg 9 (5), 1–71 (in German).
- Korteweg, D.J., 1878. Ueber die Fortpflanzungsgeschwindigkeit des Schalles in Elastischen Röhren (On the velocity of propagation of sound in elastic pipes). Annu. Rev. Phys. Chem. 5, 525–542 (in German).
- Lepareux, M., 1994. Programme PLEXUS. Matériau "EAU". Modèle homogène équilibré, Tech. Rep. DRN/DMT 94.398, CEA, (in French).
- Liu, T.G., Khoo, B.C., Xie, W.F., 2004. Isentropic one-fluid modelling of unsteady cavitating flow. J. Comput. Phys. 201 (1), 80–108.
- Lochon, H., Daude, F., Galon, P., Hérard, J.-M., 2016. Comparison of two-fluid models on steam-water transients. ESAIM Math. Model. Numer. Anal. 50 (6), 1631–1657.

- Lochon, H., Daude, F., Galon, P., Hérard, J.-M., 2017. Computation of fast depressurization of water using a two-fluid model: Revisiting Bilicki modelling of mass transfer. *Comput. & Fluids* 156, 162–174.
- Mostowsky, A.F., 1929. Investigation of water hammer in pipes at low pressures, *Bulletins of the Moscow Transport Engineering Institute - in Memory of F. E. Dzerjinsky*, Vol. 11, pp. 263–304 (in Russian).
- Neuhaus, T., Dudlik, A., 2006. Experiments and comparing calculations on thermohydraulic pressure surges in pipes. *Kerntechnik* 71 (3), 87–94.
- Neuhaus, T., Schaffrath, A., 2012. Tripartite mass transfer model: development, implementation in DYVRO, verification and validation. *Kerntechnik* 77, 115–121.
- Rienstra, S.W., Hirschberg, A., 2016. *An Introduction to Aeroacoustics*. Eindhoven University of Technology.
- Simpson, A.R., 1986. Large Water Hammer Pressures due to Column Separation in Sloping Pipes (Transient Cavitation) (Ph.D. thesis), The University of Michigan.
- Simpson, A.R., Wylie, E.B., 1991. Large water-hammer pressures for column separation in pipelines. *ASCE J. Hydraul. Eng.* 117 (10), 1310–1316.
- Tijsseling, A.S., 2003. Exact solution of linear hyperbolic four-equation system in axial liquid-pipe vibration. *J. Fluids Struct.* 18 (2), 179–193.
- Tijsseling, A.S., 2007. Water hammer with fluid–structure interaction in thick-walled pipes. *Comput. Struct.* 85, 844–851.
- Toro, E.F., 2009. *Riemann Solvers and Numerical Methods for Fluid Dynamics. A Practical Introduction*, third ed. Springer.
- Toro, E.F., Spruce, M., Speares, W., 1994. Restoration of the contact surface in the HLL-Riemann solver. *Shock Waves* 4 (1), 25–34.
- Wylie, E.B., 1984. Simulation of vaporous and gaseous cavitation. *ASME J. Fluids Eng.* 106, 307–311.
- Wylie, E.B., Streeter, V.L., Suo, L., 1993. *Fluid Transients in Systems*. Prentice Hall, Englewood Cliffs, NJ.
- Zhao, M., Ghidaoui, M.S., 2004. Godunov-type solutions for water hammer flows. *ASCE J. Hydraul. Eng.* 130 (4), 341–348.
- Zheng, J.G., Khoo, B.C., Hu, Z.M., 2013. Simulation of wave-flow-cavitation interaction using a compressible homogenous flow method. *Commun. Comput. Phys.* 14 (2), 328–354.
- Zhou, L., Wang, H., Bergant, A., Tijsseling, A.S., Liu, D.Y., Guo, S., 2018. Godunov-type solutions with Discrete Gas Cavity Model for transient cavitating pipe flow. *ASCE J. Hydraul. Eng.* 144 (5), 04018017, 1–9.
- Zhou, L., Wang, H., Liu, D.Y., Ma, J.J., Wang, P., Xia, L., 2017. A second-order Finite Volume Method for pipe flow with water column separation. *J. Hydro-Environ. Res.* 17, 47–55.